4. Algorithms for precipitation nowcasting focused on detailed analysis using radar and raingauge data

4.1 Introduction

The Japan Meteorological Agency (JMA) began operating of a precipitation nowcasting system in April 1988. One of the purposes of this study is to improve products this system provides. Since the algorithms and accuracy of the products depend highly on the characteristics of observation instruments and the configuration of the nowcasting system, we first outline the JMA nowcasting system. We then describe in detail the algorithms and techniques developed in this study for detailed precipitation analysis.

The subjects included in Section 4 are:

(1) Newly determined representative values of digitized radar echo intensity levels suitable for precipitation nowcasting,

(2) A method for improving radar estimates of precipitation by comparing data from multiple radars and raingauges,

(3) Radar-estimate calibration by raingauge in view of Z-R relationship modification and appropriate correspondence between calibration targets,

(4) Evaluation of the product for detailed precipitation analysis, called Radar-AMeDAS precipitation.

4.2 Outline of the JMA nowcasting system

Japan Meteorological Agency (JMA) precipitation nowcasting system went into operation in April 1988, as one of the components of the National Weather Watch (NWW) system, which was programmed to mitigate disasters caused by heavy rainfall, such as landslides, flash floods, and debris flows. The JMA nowcasting system provides hourly precipitation charts on a 5 km grid, namely Radar-AMeDAS precipitation, hourly precipitation forecast charts up to 3 hours, radar echo intensity composite, and radar echo top-height composite, using data from conventional weather radars and a network of automated weather stations, called AMeDAS (Forecast Division, 1991; Makihara et al., 1995). These products are disseminated in digital form to local meteorological offices, TV stations, and meteorological consulting corporations about 20 minutes after each hourly observation.

Features of the JMA nowcasting system are:

(1) A network of radars with a Moving Target Indicator (MTI) filter for rejecting ground clutter;

(2) A dense raingauge network with an average spacing of nearly one station per 280 km2 employed for calibrating precipitation estimates by radar;

(3) Process domain of about 1,000 km by 3,000 km;

(4) Utilization of Numerical Weather Prediction (NWP) values for forecasts up to 3 hours ahead;

(5) Prediction in view of orographic effects often found in heavy rainfall events;

(6) A format of products identical to that of the digital topography or the digital river information issued by the Geographical Survey Institute of Japan.

The domain for the nowcasting system is shown in Fig. 4.2.1. A projection with a standard line slanting about 45° against parallels and meridians, the so-called Biased-Lambert conical projection, is employed for the least

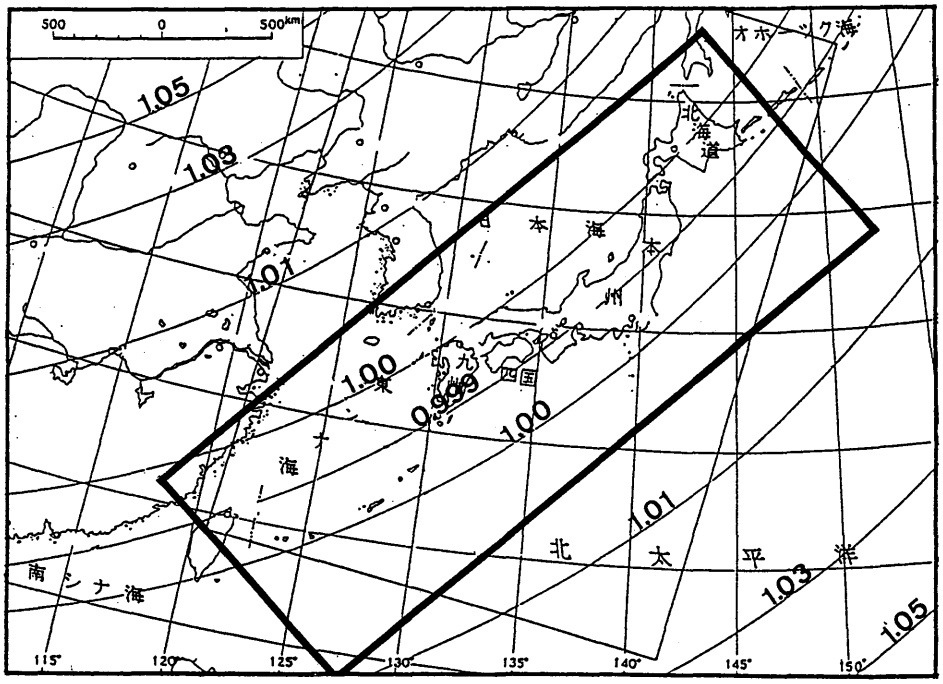

Fig. 4.2.1 Domain of the JMA nowcasting system and distortion rate on distance. The thick rectangle denotes the domain. Numbers along the thin arc lines are the distortion rates calculated by (distance on map)/ {(actual distance)/(representative fraction of map)}

distortion of direction and distance. By use of this projection, the maximum rate of distortion in the domain is about 1 % (Makihara et al., 1995).

An example of a Radar-AMeDAS precipitation chart is shown in Fig. 4.2.2, and a flowchart for on-line data processing of the nowcasting system is shown in Fig. 4.2.3.

4.3 Data

The following data are used in the JMA precipitation nowcasting system:

(1) Radar data

Echo intensity

Echo-top height

Hourly precipitation estimate

(2) Raingauge data:

Hourly precipitation

(3) NWP data

Wind forecast at 700 hPa

Wind and temperature forecast at 900 hPa

Radar data are provided by the JMA radar network, and raingauge data by a network of automated surface weather stations called Automated Meteorological Data Acquisition System (AMeDAS). With the exception of some radar data, all data are usually obtained hourly.

NWP data are used only in the forecasting process, so the detailed description is not included in this study.

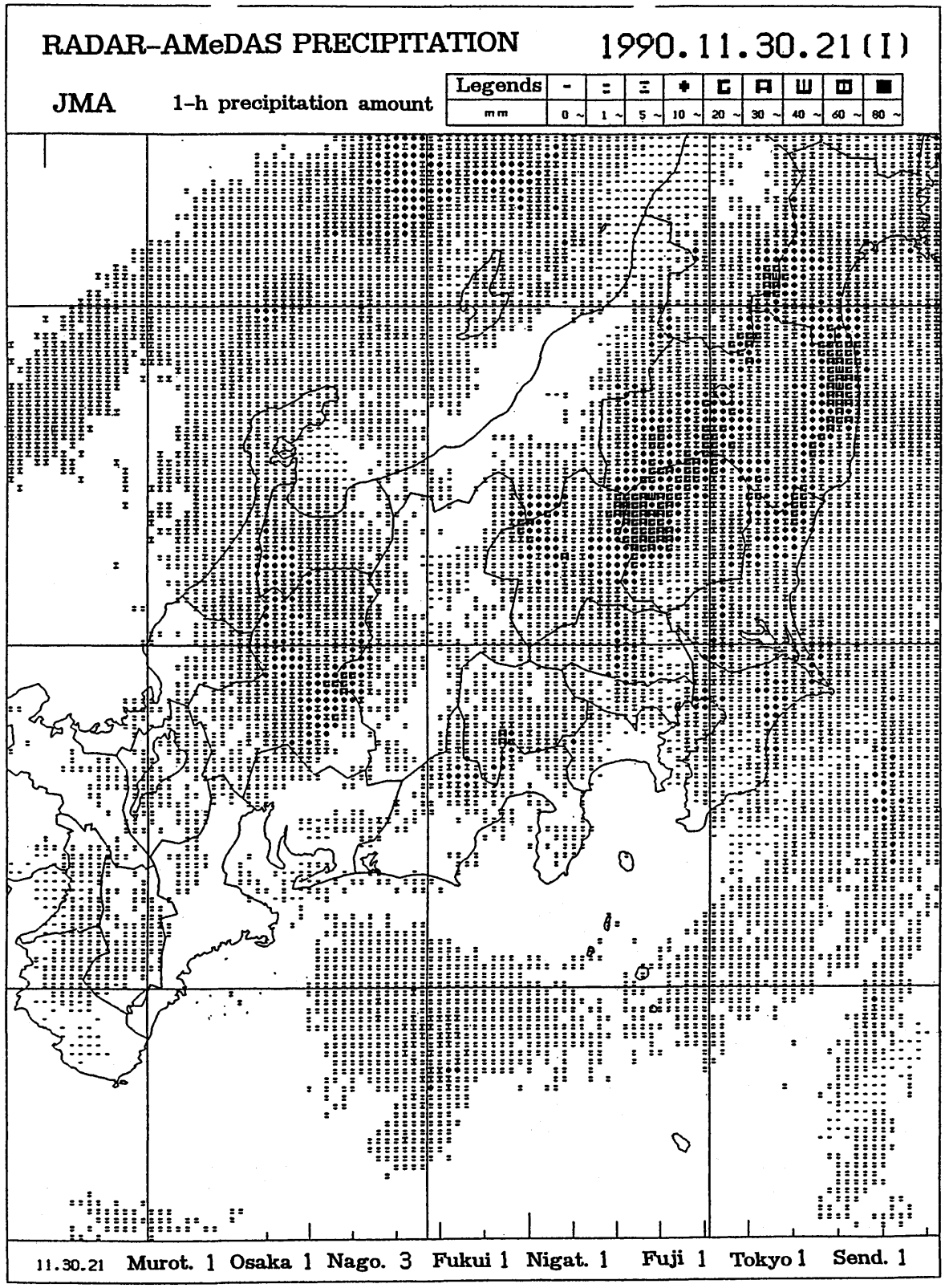

Fig. 4.2.2 Example of Radar-AMeDAS precipitation chart for Kanto district at 21 JST on 30 November 1990. The size of each pixel is 3 minutes of the latitude and 3.75 minutes of the longitude, which is equivalent to about 5.5 km by 5.5 km in this area.

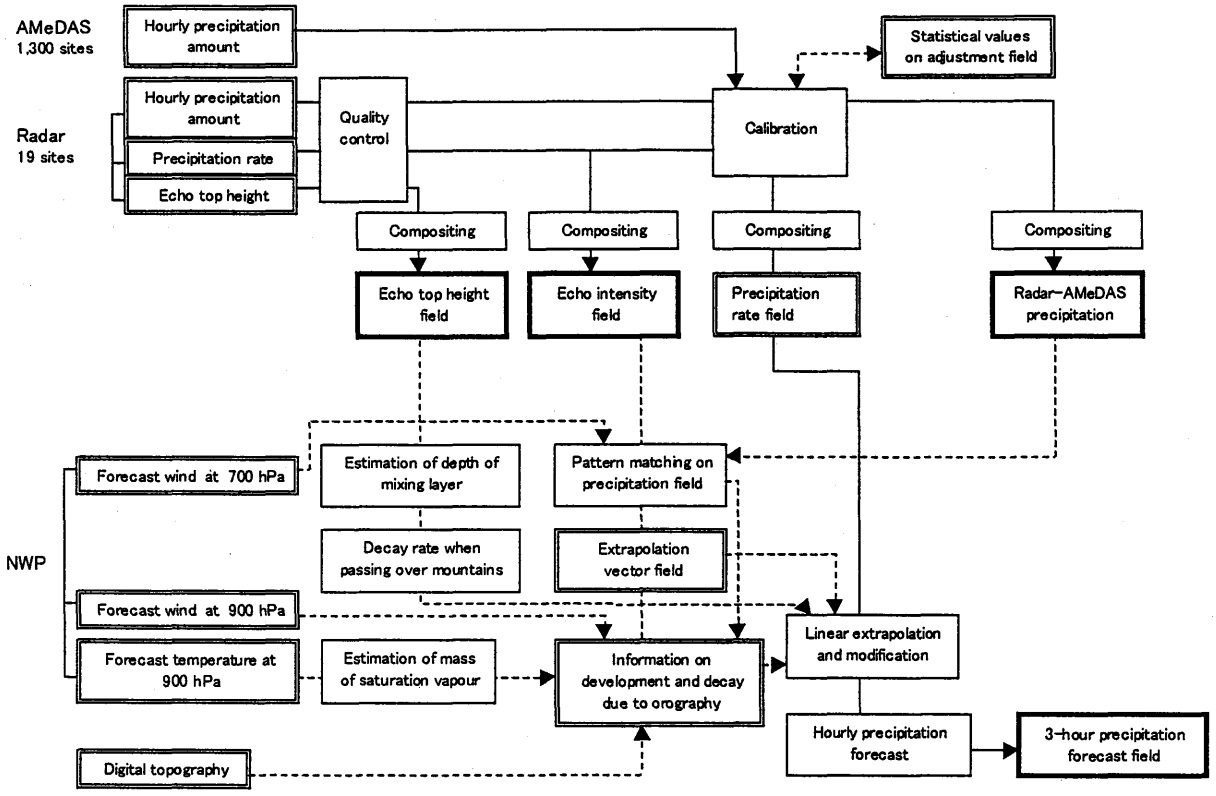

Fig. 4.2.3 A flowchart for on-line data processing of the JMA nowcasting system. Rectangles with thick line, double thin line, and single thin line denote outputs, inputs, and processes, respectively.

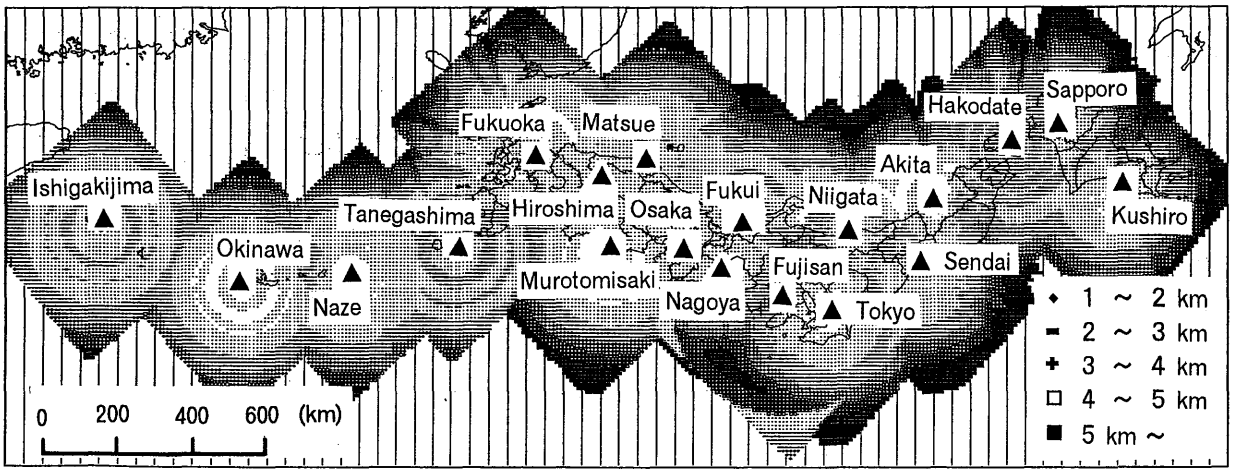

Fig. 4.3.1 JMA weather radar network. Calculation in this study is made over the unhatched area, which is the entire detection range of the radars. The observation heights of the radar beam are also indicated. The lowest value is chosen as the observation height at a pixel where more than one radar observes precipitation.

Table 4.3.1. Specifications of the radars in JMA (March 1999)

Specification	Ground-based radar for general purposes		Vessel radar
	Standard weather Radar (JMA-MR)	Mt. Fuji Radar (JMA-MR-78)	
Number of stations	18	1	1
Frequency (wave length)	5300 MHz (5.7 cm)	2880 MHz (10.4 cm)	5300 MHz (5.7 cm)
Peak power	250 kW	1500 kW	250 kW
Pulse precipitation freq.	260 Hz	160 Hz	260 Hz
Antenna diameter	3.0 m	5.0 m	2.4 m
Antenna scan speed	4 rpm	2 rpm	4 rpm
Effective range	400 km	800 km	400 km
Number of REDIS-radars	18	1	1

4.3.1 Radar data

The JMA operates 19 ground-based weather radars as of March 1999, and their entire detection range covers almost all of the Japanese Islands (Fig 4.3.1). Of these, 18 are the standard JMA type, and the other, Mt Fuji Radar, is specialized (Table 4.3.1).

An automatic data processing system, the Radar Echo Digitizing and Disseminating System (REDIS), was installed at all of these radars (Sakota, 1990). Radars with REDIS provide three types of information on precipitation, listed at the beginning of Section 4.3, for the nowcasting system with a spatial resolution of 5 km by 5 km. These data are transmitted to the Computer System for Meteorological Services (COSMETS) at JMA Headquarters through dedicated lines.

Radars with REDIS are usually operated in two observation modes: continuous and 3-hourly selected when there is little precipitation within the coverage. In continuous mode, all types of data are observed every hour. In the 3-hourly mode, only echo intensity and echo top-height are measured at 3-hour intervals. Either mode is selected manually by the operator according to the forecaster's judgment.

The JMA standard radar has the following features:

(1) 5-cm conventional radar with no Doppler processing unit

(2) Beam width of about 1.4°

(3) MTI filter installed for ground clutter rejection (Tatehira and Shimizu, 1987; Aoyagi, 1983)

(4) Height of up to 2 km for echo intensity observation with 5 low elevation angles

(5) Echo top-height estimated from observations with 14 elevations

(6) Hourly precipitation estimates accumulated at 7.5- or 10-minute intervals

The field of precipitation provided by the radar comprises a square domain on a 5-km grid with sides of 500 km (600 km for Mt. Fuji Radar). Echo intensity data from the lower five elevation angles are processed to give an echo intensity field by using an allocation chart that indicates which elevation should be selected for the value of every grid of the field. The allocation chart is made beforehand for each radar so that the altitude may be the lowest, under the condition that the radar sampling volume should not have interference by mountains, and it should not be contaminated by sea clutter.

Range correction on wave propagation and compensation for the attenuation of wave intensity by air are made

beforehand. Attenuation due to precipitation in the path of the radar, and due to a film of precipitation over the radome, is not corrected.

Echo intensity Z in the unit of dBZ is converted to a precipitation rate in the unit of mm/h by the typical relationship: $Z=200R^{1.6}$ (Marshall and Palmer, 1948).

An estimate of 1-hour precipitation by radar, a radar-precipitation amount hereafter, is produced by averaging echo intensities in mm/h, radar-precipitation rates hereafter, observed six or eight times during 1 hour.

Radar-precipitation rate, echo top-height, and radar-precipitation amount are sliced into 16, 9, and 64 levels, respectively. The original grid size of these data is 2.5km, but it is changed into 5 km before the data are transmitted to the JMA forecast center, by choosing the maximum value among four pixels of a 2.5 km-square.

4.3.2 AMeDAS

AMeDAS includes about 1,320 automatic surface weather stations. About 840 of these, called four-parameter stations, observe four meteorological parameters: 1-hour precipitation, wind direction and speed, temperature, and sunshine duration per hour. The remaining 480 have only raingauges. The density of the raingauge network is approximately one station per 17 km by 17 km. Data from these stations are collected every hour automatically and sent via public telephone lines to the AMeDAS computer center in Tokyo, where they are edited and sent to COSMETS to be introduced into the nowcasting system.

4.4 Newly determined representative values of digitized radar echo intensity levels suitable for precipitation nowcasting

4.4.1 Introduction

Continuous radar echo intensity acquired by JMA standard radars is converted into digital values which are categorized in restricted numbers of levels. The representative value for each level should not be a unique one, but should be determined according to the purpose for which the radar data are used. For example, in severe rainfall watching, the maximum in the range of a level is suitable for the purpose. In contrast, Radar-AMeDAS precipitation and very-short-range forecasts up to 3 hours are used quantitatively in the hydro-meteorological field. What values would be appropriate, for example, when we derive rainfall total or total water content for a drainage basin? Suppose the criteria be 1 mm/h, 10 mm/h, 50mm/h. In general, events near 1 mm/h occur more frequently than near 10 mm/h or 50 mm/h. Hence, rainfall total would be overestimated, if the representative value was fixed to the average of 1 mm/h and 10 mm/h, that is 5.5 mm/h, and summed in a large area or for a long period.

In this study, a set of representative values are determined in order that the statistical values of Radar-AMeDAS precipitation and very-short-range forecast may be quantitatively equal to those derived from continuous data.

4.4.2 Data

Hourly radar precipitation amounts and radar precipitation rates with a 5-km grid are used in this study. Criteria for digitizing these continuous data are listed in Table 4.4.1. Tanegashima Radar and fifteen radars to the north of Tanegashima Radar from January 1990 to October 1990 are used in this study. Data of January 1991 are used for Kushiro and Sendai Radar instead of those of January 1990 because their digitization was not completed until April 1990.

4.4.3 Method

Let the minimum and the maximum of a specific level, L, be a and b, and the frequency of a specified value x between a and b for a certain period be $f(x)$. Then, the total number of radar-precipitation amounts of L in the period, F_{ab}, is described as follows:

$$F_{ab} = \int_a^b f(x)dx \tag{4.4.1}$$

We determine representative values of L and M_{ab}, so that the total precipitation amount estimated with M_{ab} and $f(x)$ will be the same as that derived from the sum of the continuous radar-precipitation amounts, as follows:

$$M_{ab}\int_a^b f(x)dx = \int_a^b xf(x)dx \tag{4.4.2}$$

The data are accumulated for one month in this study.

4.4.3.1 Determination using gamma distribution

In order to determine the representative values, we have to know details of $f(x)$. In this study, we apply a gamma distribution, which is often used to represent rainfall distribution.

A gamma distribution is described as follows:

$$f(x) = mx^k \exp(-nx)$$

where k, m, and n are positive parameters.

In logarithmic form, the equation is described as:

$$\ln(f(x)) = \ln(m) + k\ln(x) - nx \tag{4.4.3}$$

Frequencies of hourly radar precipitation amounts for different levels are shown in Fig. 4.4.1. Approximations to these frequency distributions are made with the gamma distribution function and are also shown in Fig. 4.4.1.

As Fig. 4.4.1 indicates, frequencies for radar-precipitation amounts are well described by the gamma distribution. Those of the radar precipitation rate are described with only small errors (figures not shown). Furthermore, as three continual levels are concerned, the distributions can be well described as a linear function, and $k\ln(x)$ can be treated as constant. Under these assumptions, $f(x)$ is approximated as follows:

$$f(x) = m\exp(-nx)$$

The representative value of a specific level between the values a and $a+x$, M_{ax}, is then determined as:

$$F_{ax} = \int_a^{a+x} f(t)dt = [-m\exp(-nt)/n]_a^{a+x} \tag{4.4.4}$$

$$M_{ax} = \frac{\int_a^{a+x} tf(t)dt}{\int_a^{a+x} f(t)dt} = \frac{[t\exp(-nt)]_a^{a+x}}{[\exp(-nt)]_a^{a+x}} + \frac{1}{n} \tag{4.4.5}$$

Likewise, the frequency of the data between b and $b+y$, F_{by}, is described as:

$$F_{by} = [-m\exp(-nt)/n]_b^{b+y} \tag{4.4.6}$$

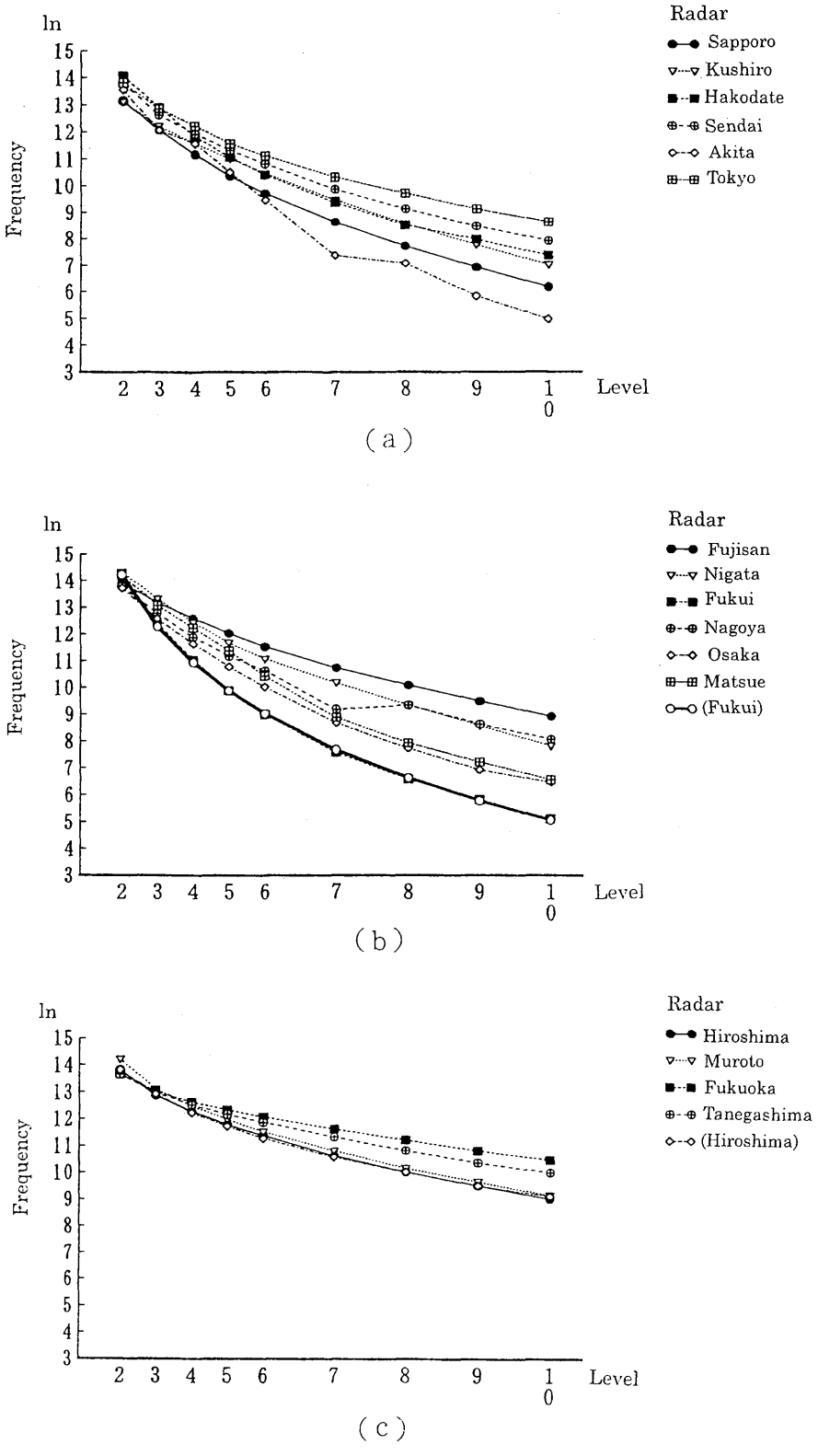

Fig. 4.4.1 Frequency distribution of hourly radar-precipitation amounts. Frequencies of each level are indicated for different radars. Data were observed in January, April, July, and October 1990. Data observed with observation height of 2 km and lower were used in the statistics. The vertical axis shows total numbers on a logarithmic scale, and the horizontal axis shows levels on a linear precipitation intensity scale.
Fukui Radar and Hiroshima Radar in parenthesis are gamma distributions to approximate the actual distribution. Parameters m, k, and n were determined with the least squares method so that difference between the actual distribution and the approximation may be the smallest. Specific values for m, k, and n for Fukui Radar and Hiroshima Radar are 14.2, 13.9, -4.7, -2.1, 0, and 0.1, respectively.

From Eqs. (4.4.4) and (4.4.6), the following equation for n is derived:

$$F_{by}[-\exp(-nx)/n]_a^{a+x} = F_{ax}[-\exp(-nx)/n]_b^{b+y} \tag{4.4.7}$$

We determine the parameter n by Newton's approximation, then, M_{ax}, a function of n in Eq. (4.4.5).

4.4.3.2 Determination of the value for the lowest level

In Eq. (4.4.2), the minimum and the maximum of a specific level must be known. However, the minimum of the lowest level cannot be fixed because the value depends on the minimum detectable power of radar signals. For that reason, we use raingauge data from AMeDAS. Actually, the right hand side of Eq. (4.4.2) is replaced with the rainfall total measured from AMeDAS raingauges.

In this method, however, radar precipitation does not always correspond to the raingauge measurement on the same grid for the following reasons:

(1) Raingauges represent values on a spot, while radar estimates spatial average values, so they sometimes differ in a severe local storm event,

(2) Raindrops aloft observed with radar sometimes drift before reaching the ground, which causes the difference of the corresponding grids between radar estimates and raingauge measurements.

To avoid this problem, the data are used only if the eight grids surrounding the center grid have the same level as the center grid.

This method is considered to be effective only when precipitation is from stratus clouds, so the method is used only for the lowest level. The difference between this method and that in 4.4.3.1 for the second lowest level is less than 0.2 mm for each radar station.

Another problem is that radar estimates are not equal to raingauge measurements. For this problem, we assume that radar estimates of the lowest and the second lowest level can be calibrated with the corresponding raingauge measurements with a parameter g as follows:

$$M_1F_1 = R_1/g \tag{4.4.8}$$

$$M_2F_2 = R_2/g \tag{4.4.9}$$

Where

M_1: representative value for level 1 (lowest level)

F_1: total number of level 1

R_1: total precipitation measured by AMeDAS raingauge

g: parameter.

The parameter g is determined by substituting M_2 that is derived from Eqs. (4.4.5) and (4.4.7) into Eq. (4.4.9).

4.4.3.3 Modification due to the change of grid size

Representative values for digitized levels of both radar precipitation rate and radar precipitation amount can be determined individually from the algorithm in the previous sections. It is considered that although fluctuations during one hour cannot be described in the rainfall rate, the total sums for the two data for a long time or for a large area should be equal. However, precipitation total from radar-precipitation rates is always larger

than that from radar-precipitation amounts if those representative values are determined individually, as Fig. 4.4.3 shows. In a very-short-range forecast, precipitation rate is used as the initial field. For using the precipitation rate in the forecast, the two sets of representative values should produce statistically the same total precipitation. In this section, the reason for this difference is discussed and a method for modification is proposed.

The primary reason for this difference is considered to be the change of the radar grid size. In general, the maximum of averages of radar precipitation rates in one-hour, that is radar-precipitation amount, is smaller than the maximum of radar-precipitation rate at any given time. For example, let an isolated echo of 10 mm/h with a size of 2.5 km square move eastward at a speed of 5 km/h, and the echo be on the grid a from time t to $t+30$ minutes. During the following 30 minutes, the echo might be on the grid 2.5 km east of a. Then, we consider the precipitation values for the period from t to $t+60$ minutes in an area including a and the grid 2.5 km east of a. The precipitation amount is calculated as 5 mm/h for two 2.5-km grids, and the precipitation rate indicates 10 mm/h at a 2.5-km grid. Although the averages of four 2.5-km grids are equal (2.5 mm/h), the maximum of precipitation rate for a 5-km grid is 10 mm/h and that of precipitation amount is 5 mm.

To make the difference clearer, the ratio of the frequency of radar observations with a 10-km grid to that with a 5-km grid for different levels is presented for radar-precipitation rates and radar-precipitation amounts in Fig. 4.4.2.

In view of the above idea, representative values of precipitation rate are modified from the upper level, in order, so that the precipitation totals from the highest to the specific level may be the same.

4.4.4 Results

4.4.4.1 Difference between central values and representative values

Table 4.4.1 shows the resulting representative values. For reference, central values are also indicated. Representative values for radar-precipitation amounts, which are determined in Sections 4.4.3.1 and 4.4.3.2 are smaller than central values by 1 to 4 %, and those for radar-precipitation rates by 2 to 9 %. Representative values for radar-precipitation rates to be used in forecast are smaller by 15 to 25 %.

4.4.4.2 Difference between precipitation total from radar precipitation rate and that from radar-precipitation amount

Figure 4.4.3 shows the ratio of precipitation total estimated from radar-precipitation rates to that from radar-precipitation amounts for each radar station. About 20 % overestimation is improved to 3.5 % by the process in Section 4.4.3.3. For several radar sites such as Hakodate, Akita, and Murotomisaki, a change of the representative value of the lowest level in view of different minimum detectable powers of radar signals further improves the overestimation.

4.4.5 Conclusions

Continuous values of 1-hour precipitation amounts and precipitation rates that JMA radar provides are digitized into 64 and 16 levels. For using these digital data quantitatively with JMA nowcasting system, appropriate sets of representative values for digital levels have been proposed.

The resulting representative values have the following features.

(1) Central values for radar-precipitation amount overestimate the actual precipitation by 1 to 4 %, while the determined values are statistically almost the same as the actual ones.

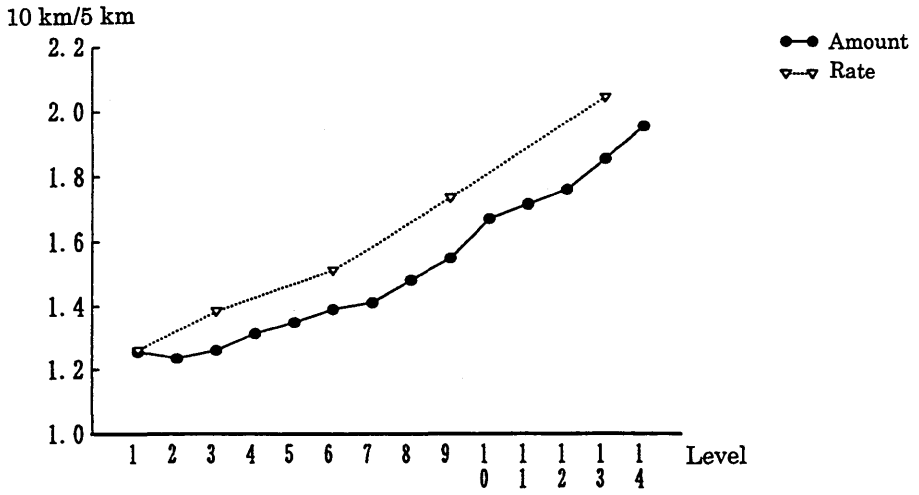

Fig. 4.4.2 Ratio of frequency of radar observations with 10-km grid to that with 5-km grid for different levels. Numbers of 10-km grid are calibrated with the factor of 4 since the total number of grids decreased to 1/4. The horizontal axis shows levels for 1-hour radar-precipitation amount.

Table 4.4.1. Radar observation levels and representative values

One-hour radar-precipitation amount				Radar-precipitation rate				
Level	Range (mm/h)	Central value	New Value[1]	Level	Range (mm/h)	Central value	New Value[1]	New Value[2]
1	< 0.5	0.25	0.30	1	< 1.0	0.75	0.67	0.67
2	0.5-	0.75	0.72					
3	1.0-	1.25	1.22	2	1.0-	1.50	1.42	1.28
4	1.5-	1.75	1.73					
5	2.0-	2.25	2.23	3	2.0-	3.00	2.82	2.45
6	2.5-	2.75	2.73					
7	3.0-	3.50	3.45					
8	4.0-	4.50	4.46	4	4 0-	6.00	5.46	4.40
9	5.0-	5.50	5.46					
10	6.0-	6.50	6.47					
11	7.0-	7.50	7.47					
12	8.0-	8.50	8.47	5	8.0-	10.00	9.67	8.40
13	9.0-	9.50	9.47					
14	10.0-	11.00	10.91					
15	12.0-	13.00	12.92	6	12.0-	14.00	13.79	12.40
16	14.0-	15.00	14.93					
17	16.0-	17.00	16.94	7	16.0-	20.00	19.41	16.80
18	18.0-	19.00	18.94					
19	20.0-	21.00	20.95					
20	22.0-	23.00	22.95					
21	24.0-	25.00	24.96	8	24.0-	28.00		24.80
				9	32.0-	36.00		32.80
40	62.0-			10	40.0-	44.00		40.80
41	64.0-			11	48.0-	52.00		48.80
42	68.0-			12	56.0-	60.00		56.80
				13	64.0-	72.00		65.60
63	152.0-			14	80.0-	88.00		81.60
				15	96.0-	126.00		99.20

Note: New value[1] indicates results by the algorithm in Sections 4.4.3.1. and 4.4.3.2, and New value[2] denotes those in Section 4.4.3.3.

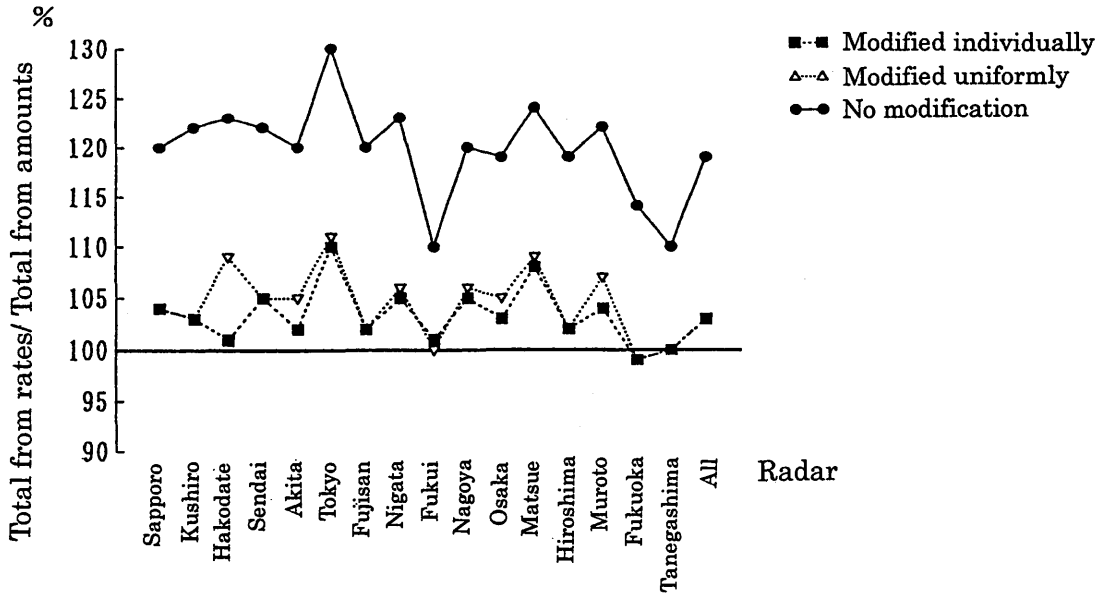

Fig. 4.4.3 Ratio of precipitation total calculated with radar-precipitation rates to that with 1-hour radar-precipitation amounts. The solid line, the dotted line, and the broken line show the ratio that used representative values derived in Sections 4.4.3.1 and 4.4.3.2, that used values calculated in Section 4.4.3.3, and the ratio that used values in Section 4.4.3.3 with the lowest level individually determined for every radar, respectively.

(2) Central values for radar-precipitation rate overestimate the actual by 15 to 25 %, and new values about 3.5 %. The main reason for excessive central values is considered to be due to the change of the grid size and the adoption of the maximum as the representative of four 2.5-km pixels.

Individual values in actual situations vary in the extent that the same level allows, which means newly determined representative values are not always appropriate. However, in estimating areal precipitation total and precipitation for a long time or for a large area, the representative values that this study proposes might reduce statistical errors of those data.

4.5 A Method for Improving radar estimates of precipitation by comparing data from multiple radars and raingauges

4.5.1 Introduction

With the capability of continuous observation of precipitation over a wide area, as well as the facility for real-time processing, weather radars are being utilized not only in the meteorological field, but also in the hydrological field. To meet hydrological needs, however, the quantitative accuracy of radars, especially those under constant operation, requires some improvement when compared with that of raingauges.

Studies have been made intensively for improvement in the accuracy of precipitation estimates by radar. One proposal is to increase information by additional hardware. It is well known that measurement of the size distribution of the rain drops in a radar sampling volume provides a more accurate estimation of the precipitation amount in the volume. For example, Seliga and Bringi (1976) utilized polarized waves, while Doviak and Zrnic (1984) showed that the use of two different wavelengths can also determine the distribution.

Another approach is to obtain other kinds of information different from that of rain drops in the air. Brandes

(1975) calibrated a field of precipitation estimated by radar with data from densely deployed raingauges. Colier et al. (1975) investigated the effectiveness of the density of raingauges to the calibration of radar estimates. Austin (1987) stressed the importance of the change of the Z-R relationship according to the type of storm. On the other hand, Joss (1990) proposed some correction methods based on the average vertical profiles of radar echoes to obtain precipitation on the ground from the radar echo observed above the ground. Using average seasonal correction fields, Takemura et al. (1984) corrected the radar estimates of hourly precipitation over the sea to produce radar-AMeDAS precipitation charts, which were produced operationally using Japan Meteorological Agency (JMA) radars.

However, in compositing the estimates by the JMA radars, differences in intensity often arise along the borders of the domains of the respective radars, especially over the sea, even if the estimated precipitation maps are modified by the methods mentioned above.

Some of the reasons for the differences are:

1) Differences in height and volume of the radar beams which observe the precipitation having a vertical profile in which the strength of precipitation changes with height;
2) Differences among the sensitivities of radar receivers;
3) Modification made for a radar with no relation to another nearby radar;
4) Difficulty of modification by raingauges over the sea.

JMA operates 19 weather radars over an area of 370,000 km^2 with spacing about three times denser than that of NEXRAD (Golden et al., 1986). However, mountains often obstruct observations in Japan. As a result, there are some areas where the distance between an observed point and a radar site is more than 150 km, even with this dense radar network. The distance over which precipitation can be estimated accurately from the radar equation without any problems, such as vertical difference of distribution of rain drops or a radar sampling volume not filled up with rain drops, is within about 100 km. For larger distances, the errors described in 1) become dominant.

Regarding 2), Takase et al. (1988) pointed out that ratios of radar estimates to the corresponding raingauge measurements are often different from those by another radar even if specifications for those radars are the same. Joss and Pittini (1991) also stated a similar conclusion.

This section proposes a method for calibrating radar estimates by comparing them not only with raingauge measurements but also with radar estimates from other radars. This method eliminates the discontinuity in radar echo compositing and improves the estimates over a wide radar detection area. This method is effective for an area where errors based on the vertical profile of precipitation are dominant, especially over the sea, and for a radar echo composite which needs smooth compositing of data from different radars. In this method, a calibration factor is first described with two parameters, and the parameters are then determined by the least -squares method using hourly radar and raingauge data.

4.5.2. Data

Data of the digital radar network of the JMA from January 1990 to February 1993 are used in this study. Throughout the period, 16 digital radars (three radars in the western part of Japan were excluded) were operated, and Okinawa Radar and Naze Radar were equipped with a digital processing unit in April 1991 and April 1990, respectively (Fig. 4.3.1).

Elevations for the field of precipitation are selected so that the altitude is the lowest, under the condition that the radar sampling volume should not have interference by mountains, and it should not be contaminated by sea clutter. For the Z-R relationship, the values proposed by Marshall-Palmer (1948), that is, 200 for B and 1.6 for β, are employed (Sakota 1990).

To obtain raingauge measurements for calibration, the raingauge network of AMeDAS is used.

Calculations in this study are conducted in the domain for JMA nowcasting system.

4.5.3. Relationship between radar beam height and the statistical field of precipitation observed by radar

Joss and Waldvogel (1989) estimated the percentages of the precipitation that can be observed by a radar at various ranges for convective rain, widespread rain and snow, and low-level rain on the basis of the average vertical reflectivity profiles. Although the percentages show different distributions, they decrease as the distance from the radar increases, and the rate of decrease is larger for the precipitation with lower echo top -height. Takemura *et al.* (1984) also made a similar investigation using radar and raingauge data during 6

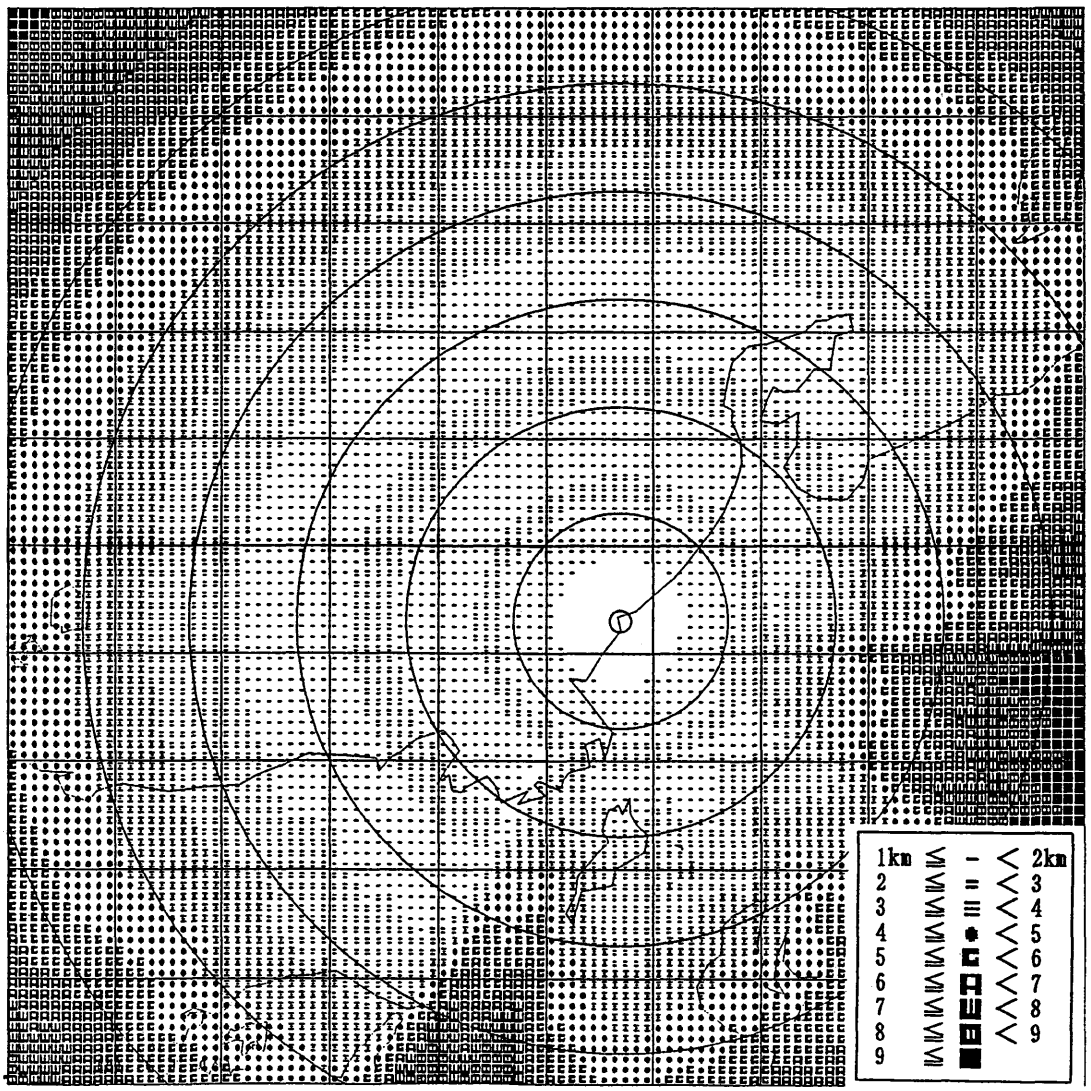

Fig. 4.5.1 Heights of the radar beam for a JMA operational radar (Fukui Radar), for observing precipitation. Three elevations, 0.0°, 1.0°, and 2.0°, are used for the observation. Range circles are drawn at 50-km intervals. Borders between the different elevations over the sea are along the arcs at about 60 km and 130 km from the radar site. The areas under 2 km of observation height are found with a ring shape around 80 km and 150 km from the radar site, and in the neighborhood of the radar site.

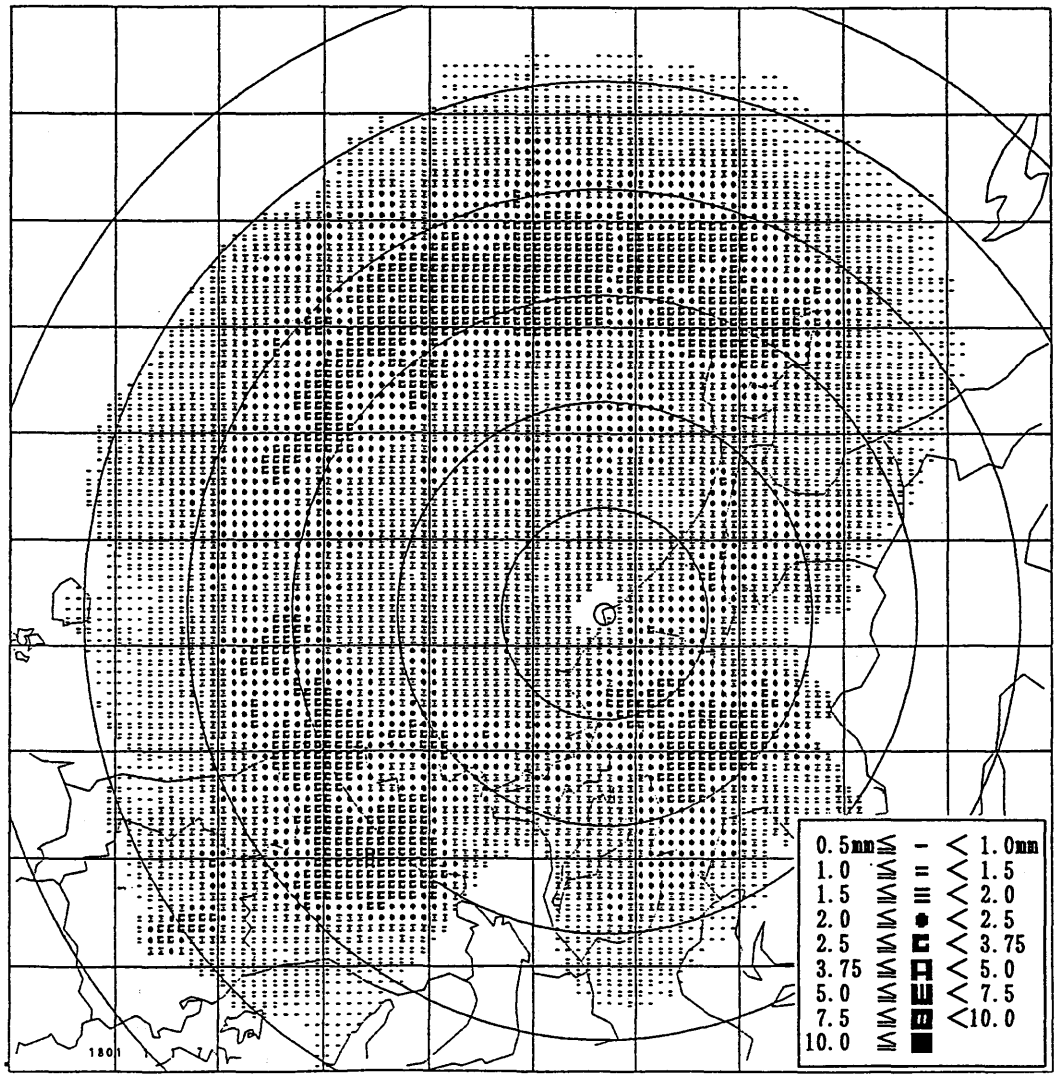

Fig.4.5.2(a) Average hourly amounts for considerable precipitation observed by Fukui Radar.
Average amounts during September 1990. Observations were usually made at 1-hour intervals, and the intervals were changed to 3 hours when there was little possibility of precipitation. The numbers in the legends indicate the average hourly amounts of precipitation estimates that were the strongest 2 % of all the observation records during the period. Range circles are drawn at 50-km intervals. Over the sea, large rates are found along a 170-km radius from the site. Another peak is found around 90-km radius. Both areas are below 2-km observation height.

months in the warm season. They pointed out that the average field of calibration factors on land showed a high correlation to the field of the minimum height through which radar beams pass without obstruction. They applied this relationship to an algorithm, and produced radar-AMeDAS precipitation maps, in which the calibration factor field for the radar was given as constant with time, except for areas where raingauges could be used for the calibration by a correction method. This relationship will be clarified by another investigation in this study.

Figure 4.5.1 indicates the field of height of the beam by which Fukui Radar, one of the JMA radars, observes precipitation. Fukui Radar was using three elevations for intensity observation with an almost constant altitude when the data in this study were observed. The heights over any area more than 130 km from the radar are of the lowest elevation because sea clutter has no influence beyond the tangent point of the beam path of

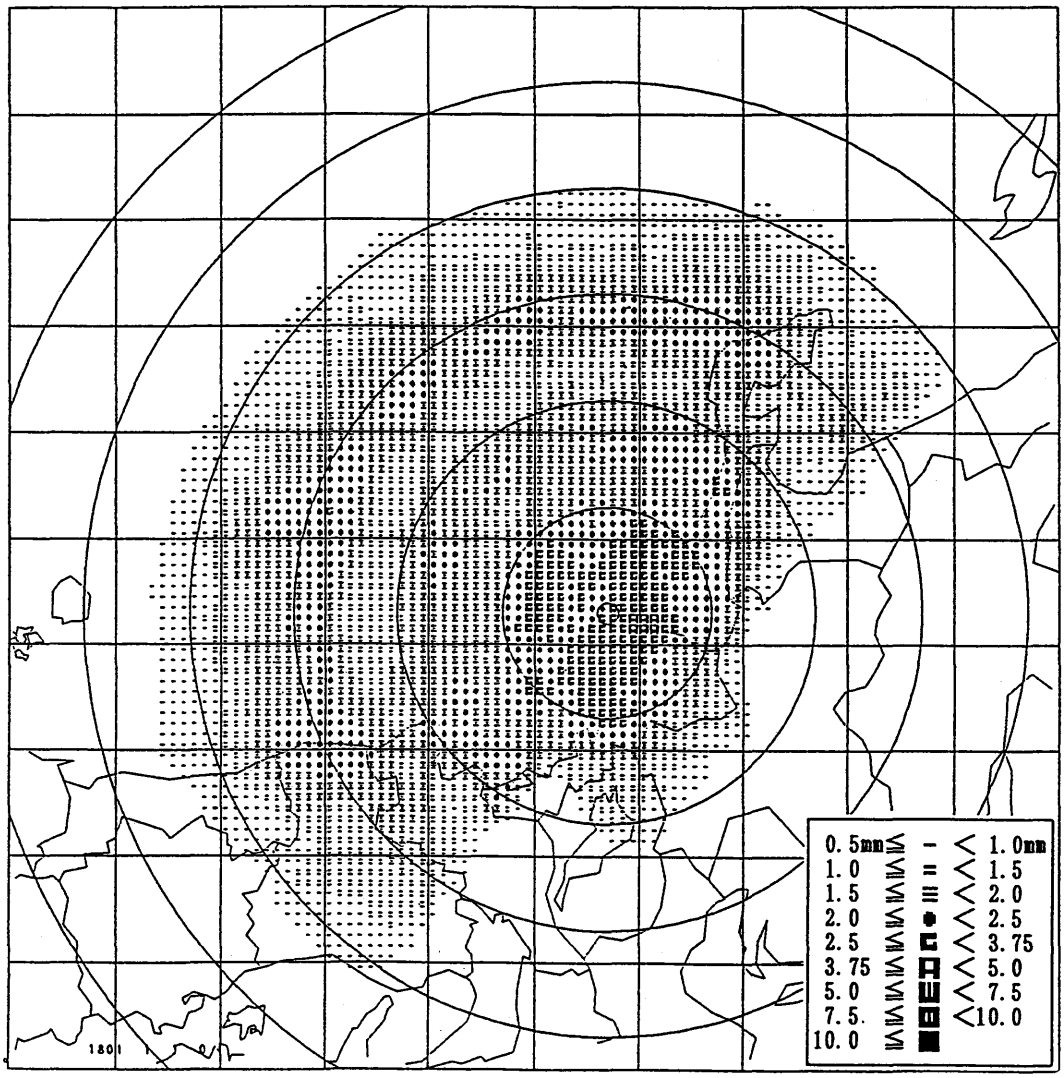

Fig.4.5.2(b) Average hourly amounts for considerable precipitation observed by Fukui Radar.
The same as (a), except during January 1990. There are areas of large amounts along 140-km and 90-km radius from the radar site. There is another maximum around the center.

Fukui Radar at the earth's surface. Around 110 km from the radar, the second highest radar beam is adopted to avoid sea clutter.

Figure 4.5.2a is the field of the averages of hourly precipitation estimates for Fukui Radar which were collected from the strongest 2 % of the observations during August 1990. In other words, it is the field of the averages of severe precipitation estimates during the month. Zero was assigned for locations where the frequency of precipitation echoes did not reach 2 % of the observations. If all of the radar estimates were accurate, the pattern would show the average precipitation amounts. However, the most obvious characteristic is that the intensities are weak in the areas with high observation altitudes. Though it cannot be denied that precipitation happens to be weak in all the areas with high observation altitude, it is natural to regard, as Joss and Waldvogel (1989) stated, that the lesser amount is caused by weaker estimates due to smaller occupancy of the radar sampling volume by rain drops, or to observing different contents of radar echoes along the vertical direction. Discontinuity around the border of different observation angles seen along a circle with a radius of 130

-km from the radar in Fig. 4.5.2 is considered to occur for this reason.

In the above investigation, only a part of the observations were used. On the grid with the higher observation altitude, not only the intensity but also the frequency of detection decreases. It is not reasonable to include those grids with very small detection rates in the data for the analysis because they may be observed only for a particular restricted condition, such as precipitation from tall clouds.

The above relationship changes with season, as shown in Fig. 4.5.2b. Because the average echo top is lower in winter, a small increase in observation height often corresponds to small occupancy of the radar sampling volume, and causes a large decrease in the precipitation estimate by radar. This result is consistent with those of Joss and Waldovagel (1989) and Takemura et al. (1984).

Now that we have investigated the nature of errors for the estimates, we consider how to modify the radar estimates observed above the ground. The following assumptions are made:

(1) The vertical profile of an observed radar echo can be described by a function;

(2) The ratio of a raingauge measurement to the corresponding radar estimate on the ground changes for various reasons, such as the variability of the Z-R relationship, or the difficulty of ideal maintenance of the sensitivity of operational radar hardware.

We represent the ratio of a raingauge measurement to the corresponding radar estimate observed, F, as

$$F = Af, \tag{4.5.1}$$

where A, which is the ratio of the actual precipitation to the corresponding radar estimate on the ground, is a parameter for assumption (2), and f, which is the ratio of the radar estimate on the ground to the radar estimate observed, is a function for assumption (1).

We can derive f in Eq. (4.5.1) from the distribution of the intensity of the radar beam and a function representing the vertical profile of an observed radar echo. The intensity of a radar beam at a specified angle is known to be described by an exponential function as follows:

$$I = 2^{-(\theta/\theta_h)^2},$$

where

θ: the angle from the center of a radar beam,

θ_h: the angle where the strength decreases to half of that at the center.

The intensity I of the radar beam illustrated in Fig. 4.5.3 is then described as:

$$I(z, y, R, B, \theta_h) = \exp[-\ln 2\{(z - B)^2 + y^2\}/\{R \tan\theta_h\}^2], \tag{4.5.2}$$

where

z: height of observation,

y: distance from the center in the direction normal to both the vertical and beam directions,

R: distance from the radar,

B: altitude of the center of the radar beam, which is calculated from the altitude of the radar site, the angle of elevation, and R, by the propagation equation.

In the above equation, the path of the radar beam is assumed to be almost horizontal.

Further we assume that the vertical profile of precipitation be denoted by:

$$V(z,T,a) = \{(T-z)/T\}^{1/a} \tag{4.5.3}$$

where

T: echo top height,

a: parameter for determining the shape of the profile.

The intensity of the profile is 1 at the ground, and 0 at the echo top-height. Figure 4.5.4 shows vertical

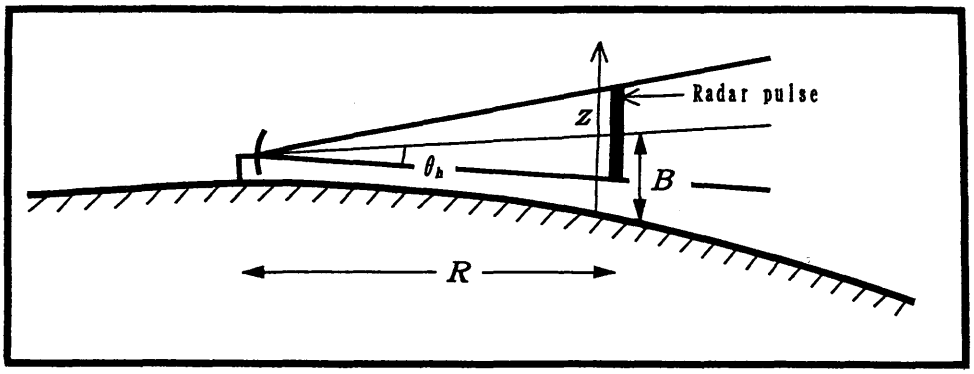

Fig. 4.5.3 Geometry of the radar beam used in Eq. (4.5.2).

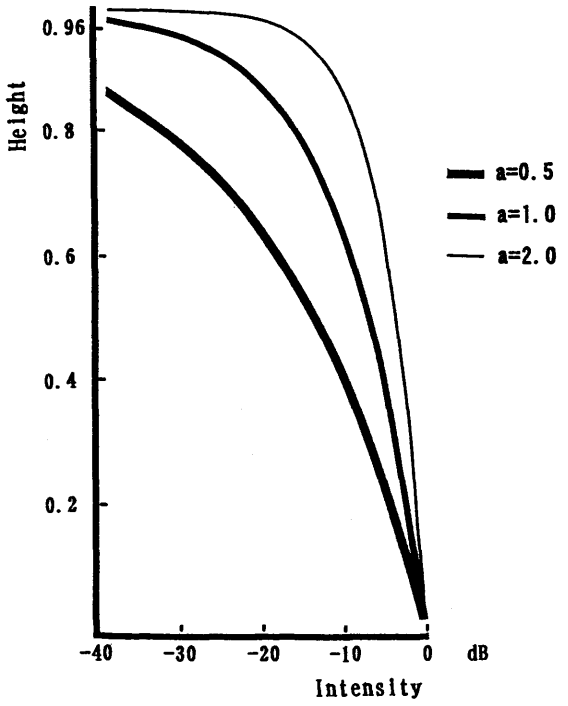

Fig. 4.5.4 Vertical profiles used for calculating the calibration factor. The vertical profile of precipitation with T km of echo top-height is described by $\{(T-z)/T\}^{1/a}$, where z is radar beam-height. In the figure, radar beam-height is described as the rate at the echo top-height. Hence, the vertical axis shows z/T. Lines in the figure are for different values of a, that is, 0.5, 1.0, and 2.0. Intensity is in dB.

profiles described by the above equation for three different values of a. When a is 1, the intensity decreases linearly in proportion to altitude; this is the assumption Andrieu and Creutin (1991) adopted for the vertical profile with no bright-band effect. By changing a from 0.5 to 2, most of the profiles investigated by Joss and Waldvogel (1989) can be approximated.

With these equations, f is represented as:

$$f(R,B,\theta_h,T,a) = \frac{\int_{B-r}^{B+r}\int_{-r}^{+r} I(z,y,r,B)dydz}{\int_{B-r}^{B+r}\int_{-r}^{+r} I(z,y,r,B)V(z,T,a)dydz} = \frac{\int_{B-r}^{B+r}\int_{-r}^{+r} \exp[\frac{-\ln 2\{(z-B)^2+y^2\}}{\{R\tan\theta_h\}^2}dydz}{\int_{B-r}^{B+r}\int_{-r}^{+r} \exp[\frac{-\ln 2\{(z-B)^2+y^2\}}{\{R\tan\theta_h\}^2}]\{(T-z)/T\}^{1/a}dydz} \quad (4.5.4)$$

where

r: size of the radar main beam defined by $R\tan(\theta_h)$.

Here, integrals are calculated for the area where the main beam passes.

In Eq. (4.5.4), the echo top-height T and the parameter a for the vertical profile are needed, and they are included as a fraction and as an integral format. Because a simple form of f is desirable for the process described later, an approximated one is proposed. Considering that f is almost 1 near the radar site, and begins to grow rapidly at a certain distance, f is approximated by the following function:

$$f(X,B) = (1+XB^2) \quad (4.5.5)$$

It should be noted that B is a function of location only, and is independent of time, while the parameter X is treated as a variable of time only.

In this approximation, θ_h is not used because it is constant for all radars. Distance R has some effect on f, although the effect is not as large as that of B. We don't include the effect of R in the approximation so that we may get sufficient results with as small a number of parameters as possible when we cannot know all of the detailed vertical profiles of radar echoes.

The parameter X represents the effect of radar sampling height and an echo profile described with T and a in Eq. (4.5.4) on the calibration factor. By introducing X, radar estimates are well calibrated when the ratio of the echo intensity observed by radar to that on the ground decreases as the radar beam becomes higher.

The function f depends on B only through its square. The form of B^2 was selected as a result of the following investigation, which was made to evaluate the performance of B to the power of different orders. For this evaluation, the correction factor described by Eq. (4.5.4) was approximated using the least-squares method. In Fig. 4.5.5, calibration factors for various distances from the radar site are approximated by three lines described as $f = (1+XB^k)$, where k is 1, 2, or 3 for the respective lines. The parameter X for each line was determined with the least-squares method to minimize total difference between the values from Eq. (4.5.4) and those from $(1+XB^k)$.

For the various situations shown in Fig. 4.5.5, where the parameter a in Eq. (4.5.3) is 0.5 and 2, and echo top

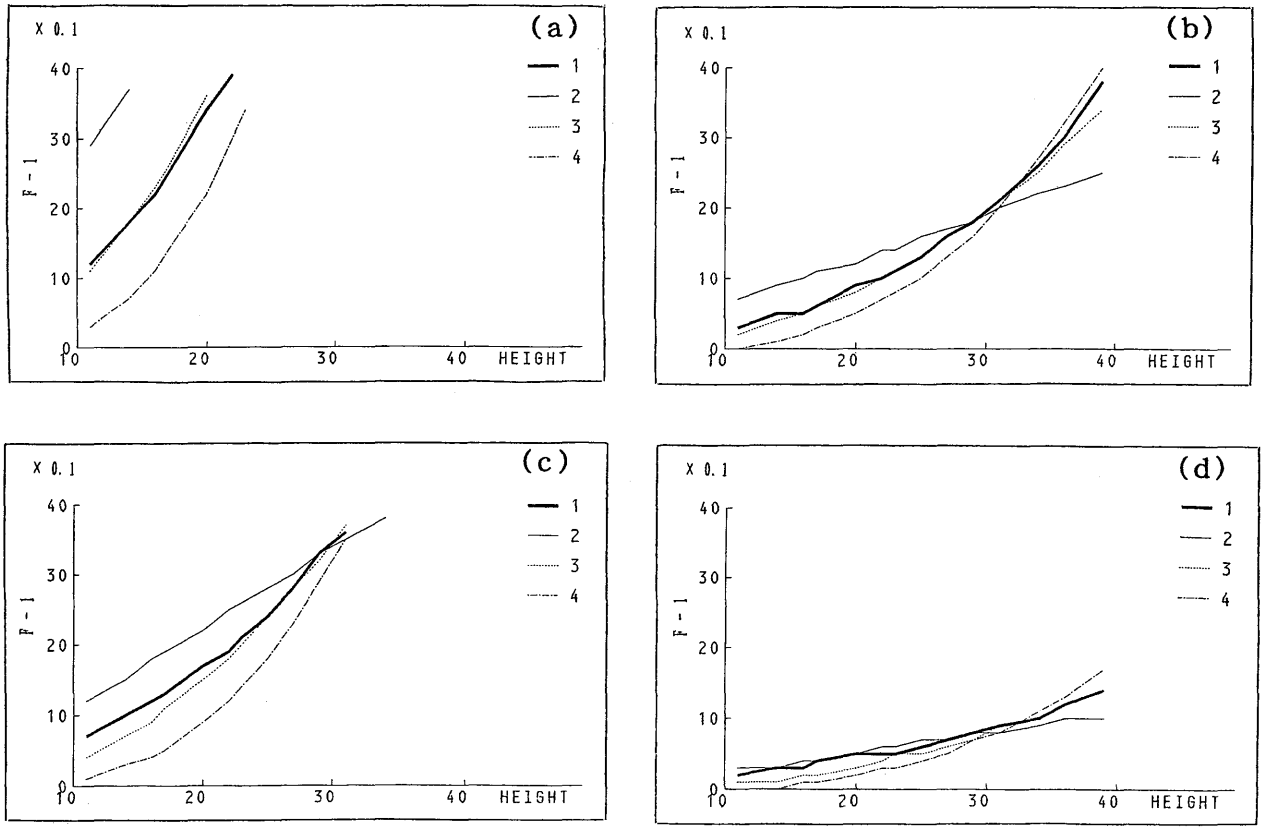

Fig. 4.5.5 Approximation to the calibration factor variable according to radar beam-height. The calibration factor calculated by Eq. (4.5.4) for the vertical profile in Fig. 4.5.4, is approximated with lines described by $1+mx^y$. The line describing calibration factors for different beam heights is denoted by number 1, and the approximations are by 2, 3, and 4, where the value of y is 1.0, 2.0, and 3.0, respectively; m for each approximated line is determined by the least-squares method so that the line may be closest to the line 1. In this study 0.7° is used for θ_h. The beam is shot from 1-km height with 0° elevation angle. The altitude of the beam becomes higher as the effect of the earth's effective radius becomes apparent. Figure 4.5.5a, 4.5.5b, 4.5.5c, and 4.5.5.d are for 4 km, 4 km, 6 km, and 6 km of echo top-height and for 0.5, 2.0, 0.5, and 2.0 of a, respectively. Comparisons for the approximation are made at 10-km intervals from the radar site for the points where the height of the radar beam is lower than 4 km.

-heights are 4 km and 6 km, the approximation with the square of B shows the least difference as a whole.

The other parameter A is also a variable of time only. JMA radars are undergoing careful maintenance, as are many others. There are, however, several difficult problems, even with the best maintenance. For example, there are large differences in the installation dates of the radars, reaching over more than 10 years in some cases, which leads to different types of parts used for the same function of those radars. As a result, it is almost impossible for the hardware, especially any working operationally, to be in strictly ideal condition for all the radars at all times. Consequently, there are errors in the measurement of the intensity reflected by raindrops. A compensation for those errors can be included in A. It should be noted that those errors are represented as a function of time only, and independent of location, although they are different among the respective radars.

Variability of the Z-R relationship also affects A. The variability is considered as a function of location, so A, which is constant for the entire detection area of the radar, cannot represent a detailed distribution of the

calibration factor field. However, A can be changed for the variability in different storm types which are almost identical in their detection area and change gradually with time. Thus, this variability is better described by being included in A as the average value at the current time.

Consequently, F in Eq. (4.5.1) is described as a function of A, X, and B by combining Eq. (4.5.5) as follows:

$$F(A,X,B) = A(1+XB^2) \tag{4.5.6}$$

4.5.4. Algorithm

4.5.4.1. Necessary conditions for the calibrating parameters

The following conditions are proposed for parameters As and Xs defined by Eq. (4.5.6), which different radars should satisfy.

1) Since radars have several errors in observation, precipitation estimates from different radars for a point where radar observations overlap are, in general, different. Their modified values, however, should be equal:

$$A_a(1+X_aB_{ak}^2)E_{ak} = A_b(1+X_bB_{bk}^2)E_{bk} \tag{4.5.7}$$

where

B_{ak}: radar beam height of Radar a at the k-th point,

E_{ak}: estimate of 1-hour precipitation amount by Radar a, at the k-th point.

Because the number of such points is usually not small, the following sum of the differences between both sides of Eq. (4.5.7) in the whole overlapping area, described as $J_1(X,A)$, should be a minimum:

$$J_1 = \sum_a \sum_{b\neq a} \sum_k \{\ln(A_a(1+X_aB_{ak}^2)E_{ak}) - \ln(A_b(1+X_bB_{bk}^2)E_{bk})\}^2 \tag{4.5.8}$$

$$= \sum_a \sum_{b\neq a} \sum_k \{A_a' - (A_b' + \beta_{abk})\}^2 \tag{4.5.9}$$

where

$$A_a' = \ln(A_a),$$
$$\beta_{abk} = \ln[\{(1+X_bB_{bk}^2)E_{bk}\}/\{(1+X_aB_{ak}^2)E_{ak}\}$$

The major reason for adopting the logarithm in Eq. (4.5.8) is to avoid unreasonable solutions. If Eq. (4.5.8) were described without the logarithm, zero might be another solution for all As, and in most cases with some residue for J_1, zero might be the only solution, which means all of the modified radar estimates become zero. The logarithm might tend to place a high weight on a small precipitation rate in determining the correction factor. However, a small estimate of a radar is not always small when it is observed by another radar, and this tendency can be modified, if necessary, by placing a high weight on samplings with a large precipitation rate, to a certain extent.

2) By transforming Eq. (4.5.7), the following relationship is obtained:

$$\{(1+X_aBa)E_{ak}\}/\{(1+X_bB_{bk}^2)E_{bk}\} = A_b/A_a \tag{4.5.10}$$

The right-hand side of Eq. (4.5.10) is composed of parameters independent of location, and the number of the

points that should satisfy Eq. (4.5.10) is not small. In other words, the value of the left-hand side, representing the ratio of a modified estimate from Radar a to that from Radar b, is constant for all the overlapping area after modification by X. It directly represents the condition that should be satisfied by estimates modified for the vertical differences. Under this condition, the standard deviation of the samples of the left-hand side for the overlapping points should be the minimum. The following should also be taken into account before the formulation of this condition:

(1) A small average of the left-hand side can also make this standard deviation small. For this reason, the magnitude of the average should be normalized.

(2) Since the situation is the same for Radar a and Radar b, it is desirable for the constraint for each of them to be equal.

Consequently, we adopt the following $J_2(X_a, X_b)$ as the value which should be minimum:

$$
\begin{aligned}
J_2(X_a, X_b) = & \frac{\frac{1}{K}\sum_k (a_{ak}/b_{bk})^2 - \{\sum_k (a_{ak}/b_{bk})/K\}^2}{\{\sum_k (a_{ak}/b_{bk})/K\}^2} \\
& + \frac{\frac{1}{K}\sum_k (b_{bk}/a_{ak})^2 - \{\sum_k (b_{bk}/a_{ak})/K\}^2}{\{\sum_k (b_{bk}/a_{ak})/K\}^2} \\
= & K\frac{\sum_k (a_{ak}/b_{bk})^2}{\{\sum_k (a_{ak}/b_{bk})\}^2} - 1 + K\frac{\sum_k (b_{bk}/a_{ak})^2}{\{\sum_k (b_{bk}/a_{ak})\}^2} - 1
\end{aligned}
\tag{4.5.11}
$$

where

$$
\begin{aligned}
a_{ak} &= (1 + X_a B_{ak}^2) E_{ak} = E_{ak} + h_{ak} X_a, \\
b_{bk} &= (1 + X_b B_{bk}^2) E_{bk} = E_{bk} + h_{bk} X_b, \\
h_{ak} &= B_{ak}^2 E_{ak},
\end{aligned}
$$

K: total number of points, k.

In deriving Eq. (4.5.11) from Eq. (4.5.10), the logarithm was not employed. This is based on the nature of X. The parameter X modifies mainly the estimates that are observed with a high beam-elevation although A modifies all of the estimates with the same weight. In order to place a large weight on data with large deviations, which is attributed mainly to samples with a high beam-elevation, we have not adopted the logarithm, because it causes a lower evaluation of the data with large deviations.

It should be noted that the objective values for Xs in J_2 are generally different from those in J_1, although both J_1 and J_2 are based upon Eq. (4.5.7)

The constraint on J_2 directly determines Xs, so Xs can modify the vertical differences of radar estimates. On the other hand, J_1 fixes Xs as one of the components that modify estimates from different radars into those with the least differences from each other. For example, let us consider three overlapping points. The value of J_2 is not, in general, zero simply because the number of parameters is two, while J_1 can be zero with four

parameters. When Xs determined by J_2 are used, J_1 cannot be fixed to zero because β_{abk} in Eq. (4.5.9) cannot be treated as constant owing to the deviation still remaining for modified samples. Therefore, the values of Xs for J_2 are different from those of J_1. In order to be accurate for the entire radar-detecting area, which includes points where radar observations do not overlap, Xs determined by J_2 are considered better than those by J_1.

3) On a grid where an AMeDAS station is located, the calibration factor should equal the ratio of the AMeDAS measurement to the radar estimate:

$$A_a(1+X_aB_{ai}^2)=R_{ai}/E_{ai} \tag{4.5.12}$$

where

R_{ai}: raingauge reading at the i-th point in the detection range of Radar a,

A_a: A for Radar a,

X_a: X for Radar a,

B_{ai}: radar beam height of Radar a at the i-th point,

E_{ai}: estimate of 1-hour precipitation amount by Radar a at the i-th point.

Because there are many AMeDAS stations to be compared within the land area of one radar's detection range, the following summation, $J_3(A,X)$, obtained by transformation of Eq. (4.5.12) should be a minimum:

$$J_3=\sum_a\sum_i[\ln\{A_a(1+X_aB_{ai}^2)\}-\ln(R_{ai}/E_{ai})]^2 \tag{4.5.13}$$

$$=\sum_a\sum_i(A_a'-\delta_{ai})^2 \tag{4.5.14}$$

where

$$A_a'=\ln(A_a),$$
$$\delta_{ai}=\ln[R_{ai}/\{(1+XB_{ai}^2)E_{ai}\}].$$

Since Eq. (4.5.13) directly compares estimates with the actual measurements, Xs and As can be derived only by this equation. The areas for this comparison, however, are limited to land only, and there are much fewer points for comparison than for Eq. (4.5.8) or Eq. (4.5.11).

4.5.4.2. Outline of the procedure

For the procedure in this study, Xs are determined firstly by Eq. (4.5.11) only, according to the consideration in Section 4.5.4.1. Then, As are derived using Eqs. (4.5.9) and (4.5.14) (Fig. 4.5.6).

Uncertainty still remains, however, in determining the parameters, even after Eqs. (4.5.9), (4.5.11), and (4.5.14) are defined. One uncertainty is in determining what weights are given to Eqs. (4.5.9) and (4.5.14) in deriving As. The other is that points of sampling are not specified. If we take all the overlapping points of the samples for Eq. (4.5.11), when most Bs are low, data with a high beam-altitude may contribute little to determining X. This X may cause large errors in areas with a high sampling altitude. Detailed strategies for weighting and for selecting samples are described in the following sections and appendices.

To better understand the procedure, Fig. 4.5.7 presents the idea and a schematic explanation of the calibration for X and A.

4.5.4.3. Determination of X by successive approximation

4.5.4.3.1. Relationship between two Xs

The determination of Xs starts by deriving the relationship between only two radars.

Let the specified radars be a and b, and X_b be fixed to X_b^* as known. The first estimate of the successive approximation, X_b^*, is obtained by averaging the data for the last 240 hours, with higher weighting for the last 6 hours. The most appropriate X_a for X_b^* is derived from the actual comparison of J_2's for various values of X_a having differences of at least 0.005 from each other. We now describe the most appropriate X_a and J_2 as $X_a^*(X_b^*)$ and $J_{2a}(X_b^*) = J_{2a}(X_a^*(X_b^*), X_b^*)$, respectively.

Taking into account that X_a^* derived in this process depends on the value of X_b^*, we calculate three different X_a^*'s and J_{2a}'s for $X_b^*-\Delta$, X_b^*, and $X_b^*+\Delta$, respectively, where Δ is a small positive number.

4.5.4.3.2. Estimation of all Xs using the relationship between two radars

Let X_b^* be the minimum of J_2a's among the three appropriate candidates in Section 4.5.4.3.1. Then, X_b^* is an appropriate estimate for X_b among them. However, we may have a different candidate, if the corresponding radar is changed from a to another. Therefore, relationships with other radars should also be taken into account. In order to include these relations for many radars in the expression in which calculation of these parameters is easy, we change the relationship between X_a and X_b into a linear one. In this expression, it is assumed that X_a can be represented as a linear function of X_b when X_b is near X_b^*. Under this assumption, the following equation for X_a and X_b is derived with two groups of X_a^* and X_b^* producing smaller J_{2a} :

$$\begin{aligned} X_a &= X_a^*(X_b^*) + \frac{X_a^*(X_b^* - \Delta) - X_a^*(X_b^*)}{\{X_b^* - \Delta\} - X_b^*}\{X_b - X_b^*\} \\ &= C_{ab}X_b + D_{ab}, \end{aligned} \tag{4.5.15}$$

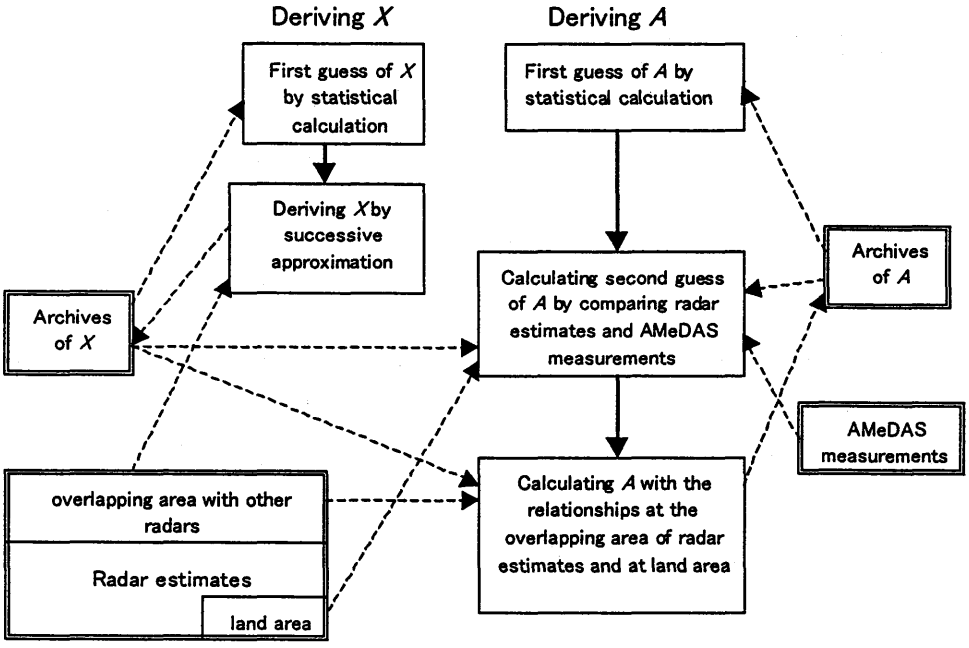

Fig. 4.5.6 Schematic flow for the algorithm for deriving X and A. Values of X are derived at first only with radar estimates and archives of X. Determination of the values of A then starts with obtaining a second guess of A, that is, the ratio of raingauge measurements to radar estimates calibrated with Xs. Finally, with this ratio and the relationship among radar estimates over their overlapping area, As, are obtained.

where both $J_{2a}(X_b^*-\Delta)$ and $J_{2a}(X_b^*)$ are assumed to be smaller than $J_{2a}(X_b^*+\Delta)$.

With Eq. (4.5.15), the same value as determined in Section 4.5.4.3.1 is derived for X_a when X_b is $(X_b^*-\Delta)$ and X_b^*.

Equation (4.5.15) can be obtained for many radars, but $X_a^*(X_b^*)$ and estimates of X_a derived from comparison

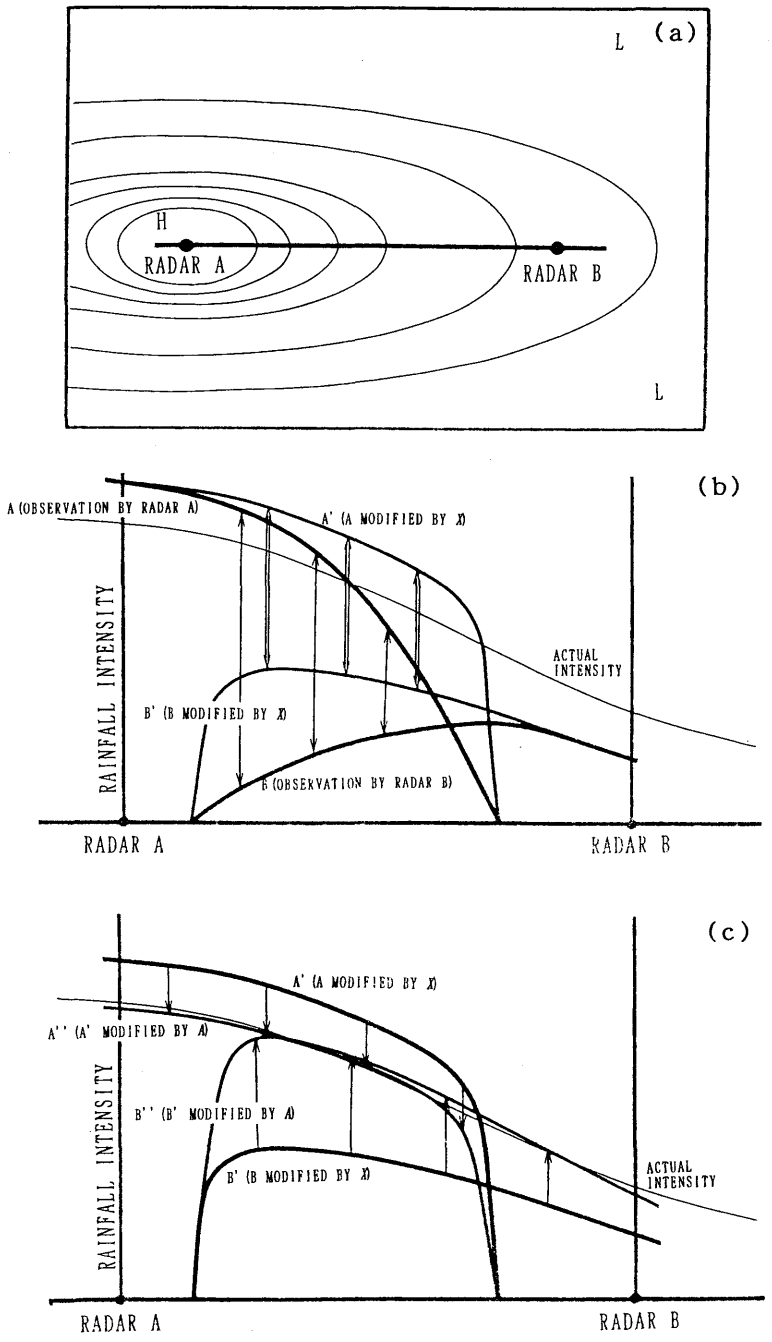

Fig. 4.5.7 Calibration methodology. Figure 4.5.7a shows an areal distribution of precipitation. A large amount is observed around Radar "A." Figures 4.5.7b and 4.5.7c are cross-sections along the thick line in Fig. 4.5.7a. Figure 4.5.7b illustrates how X modifies the original radar estimates. In the figure, the thin lines, the thick lines, and the lines with moderate thickness denote the actual intensities, original radar estimates, and estimates modified by Xs, respectively. Vertical single lines with arrows show differences between original estimates by Radar A, and those by Radar B. The parameter X modifies the estimates such that those differences can be equal without dependence of location, as vertical double lines with arrows show. On the other hand, the parameter A calibrates the estimates modified by X such that the modified lines may be along the actual intensities, as in Fig. 4.5.7c.

with many other radars are not equal. Therefore, some difference arises between both sides of Eq. (4.5.15) if an estimate of X_a, except for $X_a^*(X_b^*)$, is substituted for X_a. In view of this situation, we determine Xs such that the sum of the differences between the values of both sides of Eq. (4.5.15) for various estimates of Xs is minimum.

Actually, we obtain the following equation to describe the relationship between Radar a and Radar b in Section 4.5.4.3.1:

$$L_{2ab} = \varepsilon_{ab}(X_a - C_{ab}X_b - D_{ab})^2 + \varsigma_{ab}(X_a - M_{ab})^2 + \eta_{ab}(X_b - N_{ab})^2, \tag{4.5.16}$$

where ε_{ab}, ς_{ab}, η_{ab} are weighting coefficients, and M_{ab} and N_{ab} are X_a^* and X_b^*, respectively.

Equation (4.5.16) indicates:

(1) An appropriate pair of X_a and X_b is M_{ab} and N_{ab},

(2) Even if they differ from M_{ab} and Nab, they should satisfy the relationship of the first term described by C_{ab} and D_{ab} to keep J_2 small.

The last estimates of Xs are derived as those making minimum the total sum of L_{2ab}'s:

$$L_2 = \sum_a \sum_{b \neq a} \{\varepsilon_{ab}(X_a - C_{ab}X_b - D_{ab})^2 + \varsigma_{ab}(X_a - M_{ab})^2 + \eta_{ab}(X_b - N_{ab})^2\} \tag{4.5.17}$$

Because Eq. (4.5.17) is a quadratic format regarding Xs, the following linear equation is obtained by differentiating L_2 with respect to X_m:

$$\begin{aligned} &\sum_{b \neq m} \{(\varepsilon_{mb} + \varsigma_{mb})X_m - \varepsilon_{mb}C_{mb}X_b + (-\varepsilon_{mb}D_{mb} - \varsigma_{mb}M_{mb})\} \\ &+ \sum_{b \neq m} \{-\varepsilon_{mmb}C_{bm}X_b + (\varepsilon_{mm}C_{bm}^2 + \eta_{ab})X_m + (\varepsilon_{mmb}C_{bm}D_{bm} - \eta_{abm}N_{bm})\} = 0 \end{aligned} \tag{4.5.18}$$

Consequently, Xs are determined by solving the above simultaneous linear equations. The actual weighting strategy is described in Appendix (1).

4.5.4.3.3. Iteration

The values of Xs determined in the scheme from Section 4.5.4.3.1 to Section 4.5.4.3.2 depend on the first guess of Xs. To obtain more reliable values, the procedures are repeated three times, replacing the first guesses X_b^* by the estimates determined by Eq. (4.5.18).

4.5.4.4. Derivation of A

In order to obtain As satisfying both relationships of Eqs. (4.5.9) and (4.5.14), we propose the following form for the target of the least-squares method:

$$J_4 = \sum_a \sum_{b \neq a} \sum_{k(a,b)} \alpha_a \{A_a' - (A_b' + \beta_{abk})\}^2 + \sum_a \sum_i \gamma_a (A_a' - \delta_{ai})^2 \tag{4.5.19}$$

Then the following linear equation is derived on A_m:

$$\begin{aligned} &\sum_{b \neq m} \sum_{k(m,b)} \alpha_m \{A_m' - (A_b' + \beta_{mbk})\} - \sum_{b \neq m} \sum_{k(b,m)} \alpha_a \{A_b' - (A_m' + \beta_{bmk})\} \\ &+ \sum_i \gamma_m (A_m - \delta_{mi}) = 0 \end{aligned} \tag{4.5.20}$$

It should be noted that Eq. (4.5.7), which is the basis for Eq. (4.5.9), indicates only the ratio of the values of

respective As. For this reason, if the last term in Eq. (4.5.19) were omitted, the determinant for different A'_ms in Eq. (4.5.20) would become zero, which means that As cannot be determined only by Eq. (4.5.9).

It should also be noted that if the logarithm were not adopted in Eq. (4.5.19), unsuitable values might be derived for As. If Eqs. (4.5.8) and (4.5.14) were described without the logarithm and combined together like Eq. (4.5.19), the term in Eq. (4.5.8) would cause all As to become smaller because residues for As in Eq. (4.5.8) are small only if As are small. The result would be that As would, in most cases, be smaller than those estimated from Eq. (4.5.14), unless the relationships in Eqs. (4.5.8) and (4.5.14) could be completely satisfied with no error.

Consequently, the parameter A_m is determined by solving the simultaneous linear equations (4.5.20) on As.

The way to determine an appropriate weighting for the above coefficients is described in Appendix (2).

4.5.4.5. Process in case of no data for comparison

Determining the parameters for a radar requires some radar echoes over AMeDAS raingauges, and, at the same time, observed precipitation overlapped in some areas by at least two radars.

Actually, however, in some cases these requirements are not satisfied. For example, when a rainfall area moves eastward from the far northwest to the Kyushu District, only the Fukuoka Radar can detect the area over the sea (Fig. 4.3.1 helps show the location of the specified radar). In this case, neither Eq. (4.5.7) nor Eq. (4.5.12) proposed for the algorithm is available. After a while, the radar echoes move into the detection area of

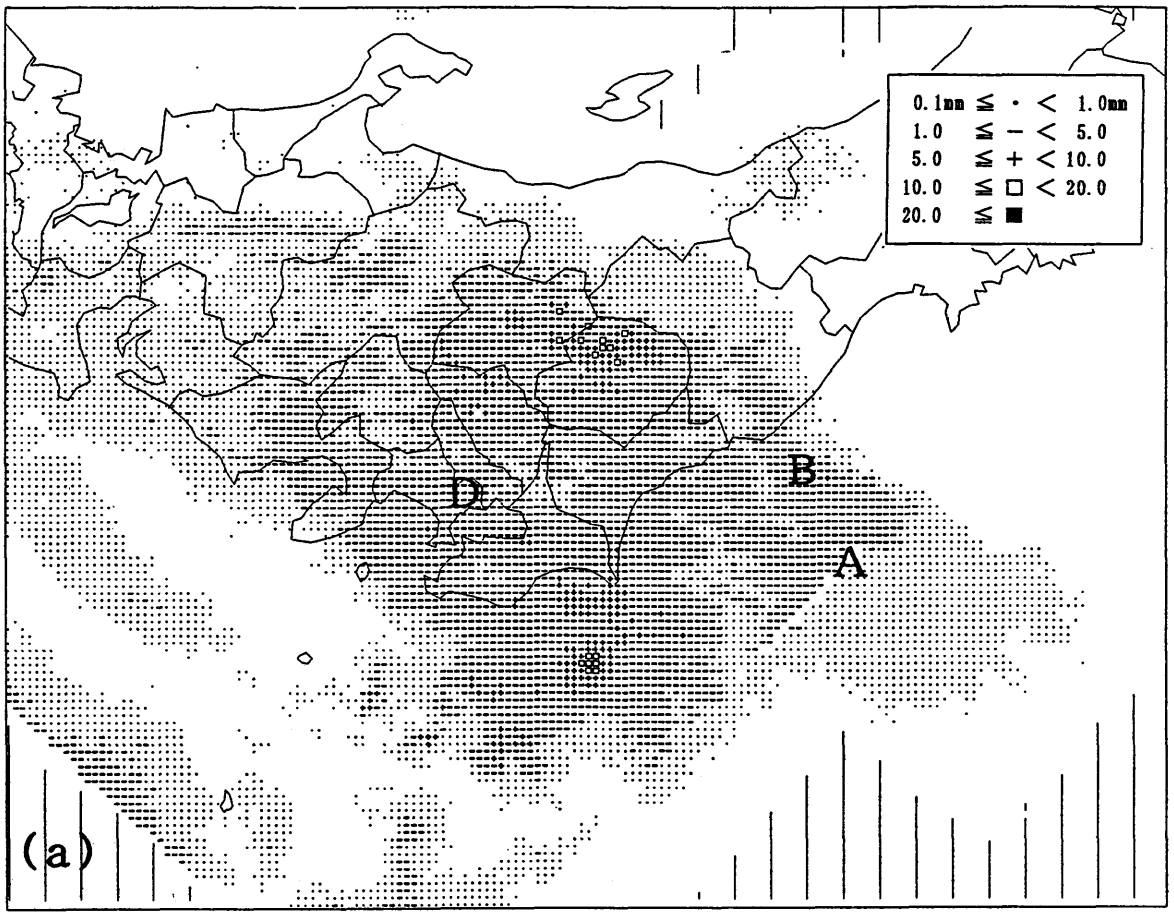

Fig. 4.5.8.(a) An example of the field calibrated with the parameters A and X.
The composite of hourly precipitation estimates by radar at 21 UTC on 27 November 1990.

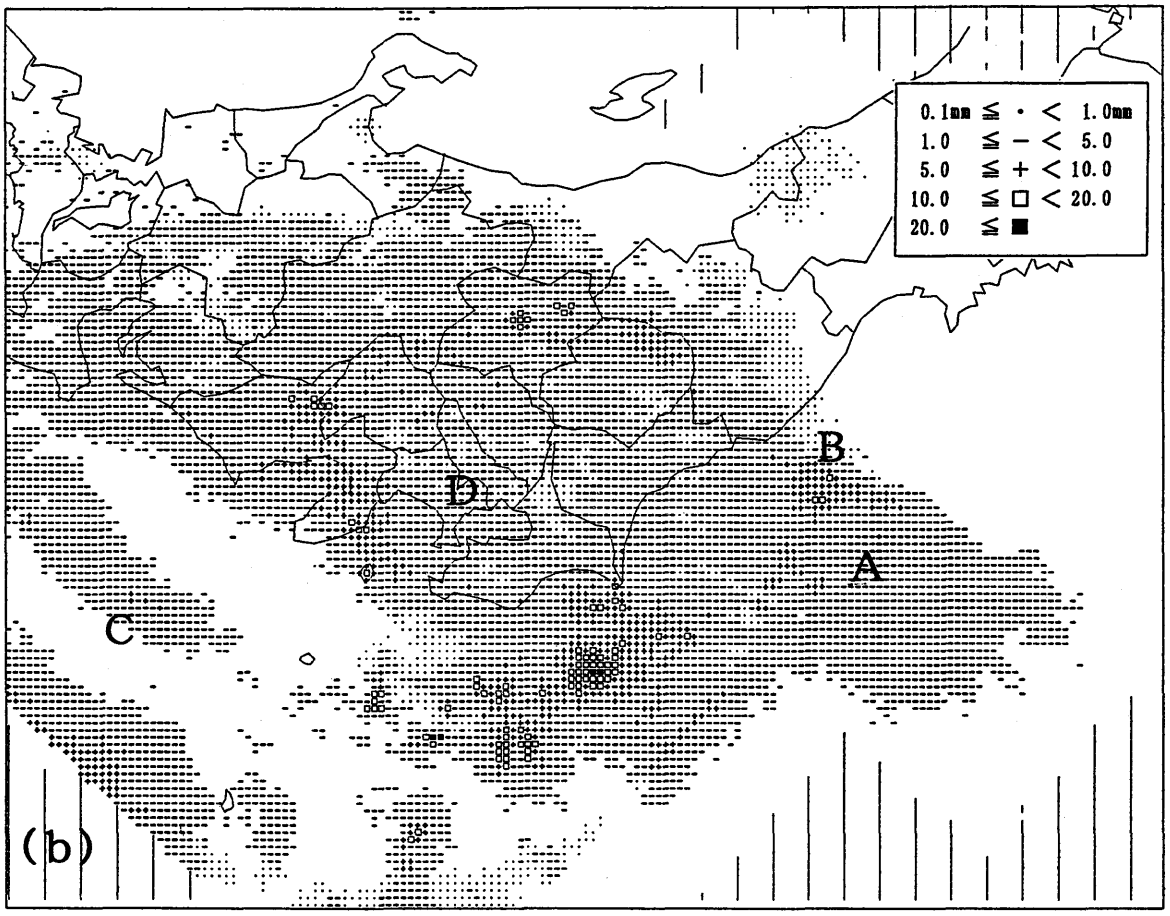

Fig. 4.5.8.(b) An example of the field calibrated with the parameters A and X.
The same as (a) except for the field calibrated with the parameters A and X. The discontinuity denoted by "A" is nearly eliminated. The intense area "B" is not clear in (a). The area "C" observed by a radar beam at a higher altitude than "D" is calibrated larger by X, and the difference between these areas has become less.

another radar, Matsue Radar. Then, with Eq. (4.5.7), Xs and the ratio of two As are determined. When the area passes over AMeDAS raingauges, As are determined with all their relationships. When some of the equations cannot be utilized, unknown parameters are supplemented with the statistical values obtained by averaging the data for the last 240 hours, with higher weighting for the last 6 hours.

It is noteworthy that if only one radar satisfies Eq. (4.5.12), all As for radars in operation can be analyzed without statistical data, although all these radars are needed to satisfy Eq. (4.5.7). In this case, however, the accuracy naturally decreases.

4.5.5. Accuracy

Figure 4.5.8a is a composite of 1-hour precipitation amounts estimated by radar at 21 UTC on 27 November 1990. The algorithm of the Forecast Division (1991) was used for compositing, and no calibration is made. In the chart, there is a clear discontinuity in intensity, denoted by "A." The left side of the area "A" is covered by three radars, and the right side, by only two radars. The different sensitivity of radar hardware primarily causes this gap. On the other hand, Fig. 4.5.8b shows one calibrated by the algorithm in this study. There is very little gap in area "A," mainly because of calibration by the parameter A. The intensive area "B," which is not clear in Fig. 4.5.8a, is represented distinctly in Fig. 4.5.8b after the calibration. The area "C," which was

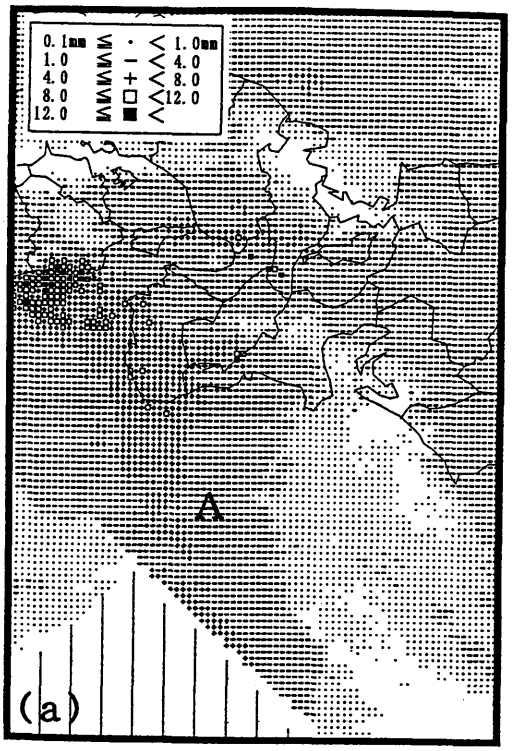

Fig. 4.5.9.(a) Effect of the parameter X.
The composite of hourly precipitation estimates by radar at 19 UTC on 16 February 1993.

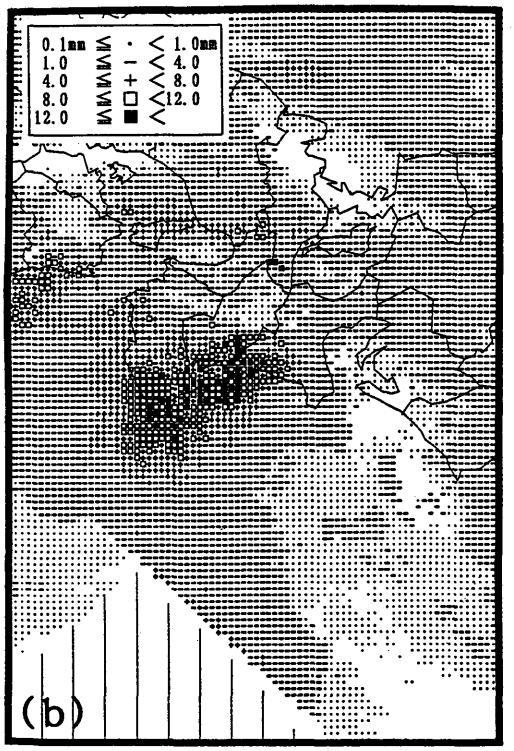

Fig. 4.5.9.(b) Effect of the parameter X.
The same as (1), except for the estimates calibrated with A and X.

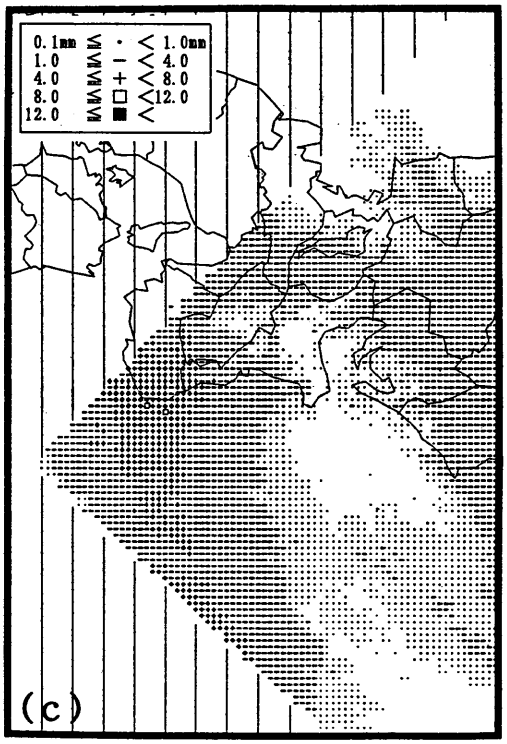

Fig. 4.5.9.(c) Effect of the parameter X.
Original estimates by Mt. Fuji Radar. The intense area with an arc shape in the center of (c) over the sea coincides with the area under 2 km of observation height shown in (e).

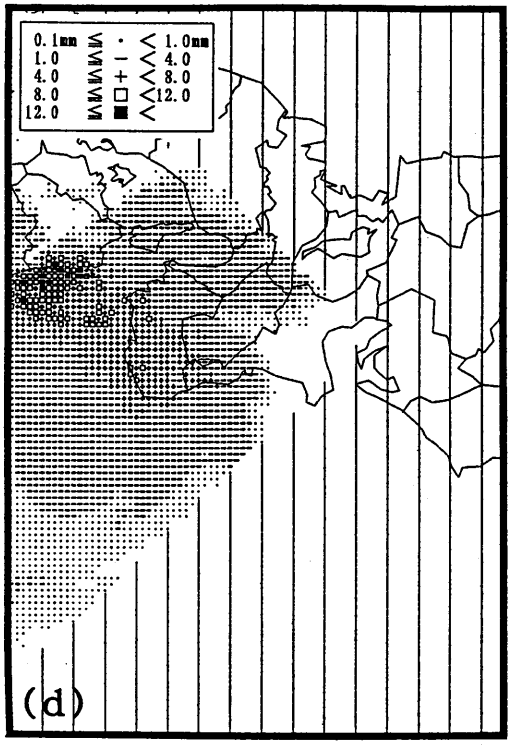

Fig. 4.5.9.(d) Effect of the parameter X.
The same as (c), except by Murotomisaki Radar located about 400 km west of Mt. Fuji Radar. The intense area in (c) is not recognized in this figure.

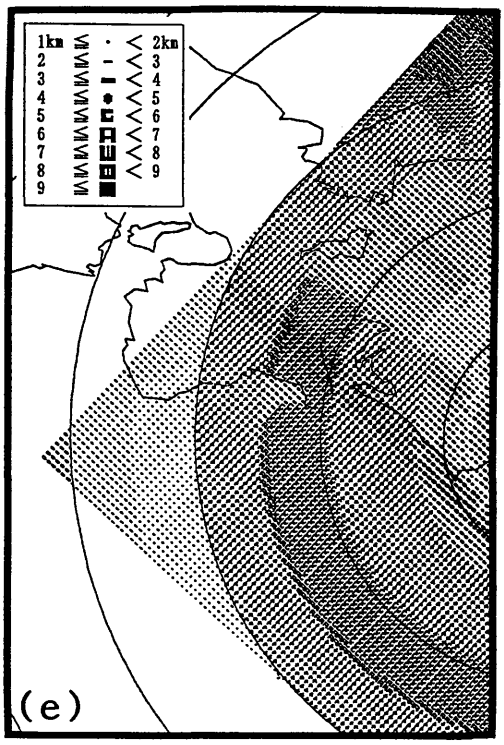

Fig. 4.5.9.(e) Effect of the parameter X.
Observation heights of the radar beam of Mt. Fuji Radar.

observed by radar at an altitude higher than area "D," has been made stronger by X, and the difference in intensity between these areas has become less.

The performance of X is explained in Fig. 4.5.9. Figure 4.5.9a is a composite of 1-hour precipitation amounts by radar with no calibration at 8 UTC on 16 February 1993, while Fig. 4.5.9b is modified using the algorithm. There is a clear difference between the figures in the area denoted by "A." For detailed verification, original estimates by two radars for the area "A" are shown in Figs. 4.5.9c and 4.5.9d. In the estimates by the Mt. Fuji Radar in Fig. 4.5.9c, there is an intense precipitation area with an arc shape. This intense area lies along the area with low observation height shown in Fig. 4.5.9e. It should be noted that the elevation angle for JMA operational radars is set higher within the tangent line, which the path of the radar beam and the earth's surface make, than beyond the line, where radar echoes are free from contamination by sea clutter. As for Mt. Fuji, there is a large difference of 1.4° between the angles on both sides of the target line. The fields of estimates by the other radars have no such distinct intense area. The algorithm for X regarded that the intense area was made by the influence of vertical variation of precipitation intensity, and the intense area was modified as Fig. 4.5.9b shows. It is noteworthy that although the area south of area "A" is not covered by any radars except Mt. Fuji Radar, the estimates there can be modified by this algorithm.

Figures 4.5.10a and 4.5.10b illustrate values of As and Xs calculated for different radars for consecutive 4-hour periods. From 18 UTC to 21 UTC on 16 February 1993, a large-scale precipitation area from a synoptic-scale depression located in the western part of Japan was moving eastward, accompanied by a weak uniform precipitation area ahead of it, and a precipitation area with convective moderate cells at its center.

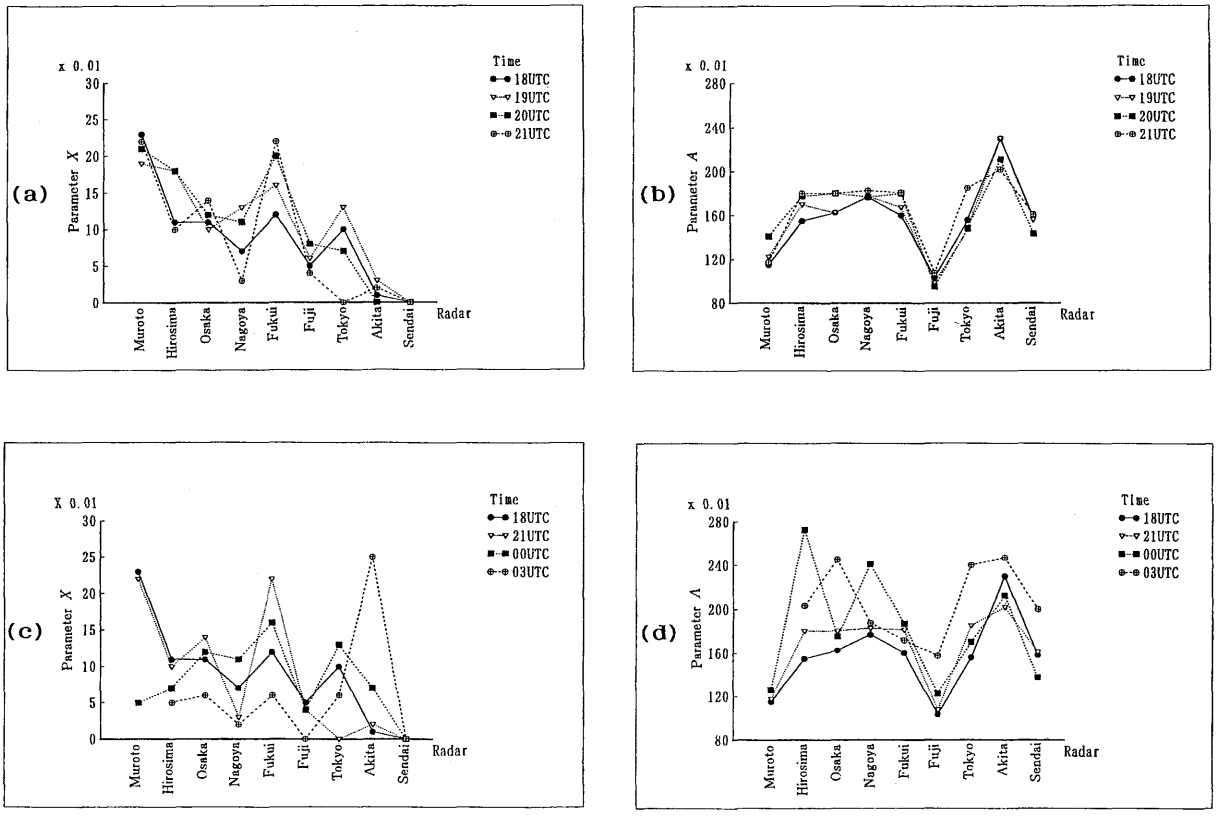

Fig. 4.5.10. As and Xs calculated for different radars and for consecutive hours.

(a) The parameter Xs calculated for 4 consecutive hours from 18 UTC on 16 February 1993. The units of X are inverse square of height in km. In the figure, radars are aligned nearly from southwest to northeast along the horizontal axis. Their actual locations are shown in Fig. 4.3.1.

(b) The parameter As for the same condition as (a).

(c) The same as (a), except for 9 hours at 3-hour intervals. Values for Akita increase with time, while those of Fukui increase for the first three samples, but decreased for the last. Only these two radars face the Japan Sea. The values for the other radars decrease.

(d) The same as (b), except for 9 hours at 3-hour intervals.

Values for X are obviously larger in the western part of Japan than in the east, although they have fluctuations. The average of the standard deviation of X for the period is 0.02. In many other case studies, more than three of the modification factors calculated about X indicated relatively larger fluctuations. The reason may be that the actual vertical profile cannot be well described in a single function for such a large ratio. It seems difficult to estimate the intensity of a radar echo near the ground when the only information is from the intensity almost at the echo top.

On the other hand, A has less areal variation in most radars. The fluctuation for A during the period is also not larger than 0.09 of the average of the standard deviation (note that the average of the values is one order larger than that for X).

In Figs. 4.5.10c and 4.5.10d, As and Xs are drawn for 9 hours at 3-hour intervals. Xs in the western part of Japan at 18 UTC was larger than in the eastern part, and became smaller at 03 UTC. On the contrary, Xs in the eastern part became larger with time. In spite of the fluctuations shown in Fig. 4.5.10a, this tendency is

clearly recognized, and it agrees with the expectation for the modification by X, that is, little modification for stratus rainfall with little vertical difference ahead of a depression, and large modification for wide-spread rainfall with some vertical difference around its center. The differences of As among radars are clearly recognized. In particular, A for Mt. Fuji Radar and for Akita radar are different from those for other radars. There is also a tendency for As to become larger with time, except for radars in eastern Japan.

Consequently, As and Xs work well for correcting errors caused by the vertical variation of precipitation intensity and the difference between radar systems.

To obtain more stable values, averaging for several hours is needed. In Figs. 4.5.8 and 4.5.9, the average of six estimates calculated at 1-hour intervals is employed.

4.5.6. Discussion

4.5.6.1. Assumption for the vertical profile

In this study, X is assumed to be the same value over the whole detecting range of a radar. Precipitation with a high echo-top is, however, observed with a smaller calibration factor than that with a lower echo-top. Actually, echo to-height contributes only a part of the denominator in Eq. (4.5.4), and this part, described as B in Eq. (4.5.3), is larger for higher echo top-heights; this situation leads to smaller f in Eq. (4.5.4). If it is effective in the detection range of a radar, the assumption for the vertical profile may become more accurate by introducing an additional parameter, that is, echo top-height. Echo top-height would be useful especially when precipitation areas would be observed by only one radar over the sea, where the estimation proposed in this study cannot be applied. More investigation is required to clarify the effectiveness and problems that may arise in adding another parameter.

4.5.6.2. Bright band effect

The model proposed in this study for modifying the vertical difference of precipitation cannot always describe the bright band effect with reliable accuracy because the thin, distinct, severe reflectivity of the bright band cannot be expressed by the parameter X. The JMA conventional radars used in this study observe precipitation by CAPPI with three or five elevation angles, and hence a distinct bright band near the radar is rarely observed in this plan-position field. As Andrieu and Creutin (1991) stated, in areas over 100 km from the radar, there is little influence from the bright band. However, further modification is desirable for a more reliable estimation, especially for the area near the radar site. It may be possible to describe the vertical profile with the bright band by adding other parameters and modifying the function proposed in this study. For example, a bell-shaped vertical variation changing according to height at which the highest reflectivity is observed owing to the bright band can be used as an additional coefficient of A, as Gray (1991) proposed. In this case, the intensity of the coefficient and the elevation of bright band should be treated as parameters to be determined. This is a theme for another development.

4.5.7. Conclusions

An algorithm that calibrates radar estimates over the whole detection area using raingauges and more than one conventional radar was proposed. In this algorithm, two parameters were used to correct two major causes of errors in estimating precipitation by radar, namely, 1) errors arising from the instability of radar hardware, and 2) the difference between the distribution of raindrops near the ground and that observed by radar over the ground, i.e. errors based upon the vertical profile of precipitation. Using these parameters and the height of the

radar beam over the target, the ratio of the actual field to the radar estimate on a grid of the field was described with a simple function. The two parameters could be calculated every hour with the least-squares method by comparing radar estimates not only with AMeDAS raingauge measurement, but also with estimates from different radars.

The use of this algorithm improved not only the discontinuity around borders of the radar coverage in the composite map, but also the discontinuity found at the borders of observation fields from different elevation angles in CAPPI of a single radar. The results from many cases showed that the algorithm was effective only when the calibration factor based on the vertical profile of radar echoes is less than about 3.

This modification has few problems for changes in the type of precipitation distribution or changes in season, because it is determined every hour from current data. This method has another advantage in that it can be used for data further from the radar than the correction method by observing the distribution of raindrops. Furthermore, one of the conditions for the algorithm, that there should be some detection areas overlapping each other among radars located at least some hundreds of km apart, is usually satisfied for most radar networks already deployed for operational use. Thus, this algorithm would help to improve radar estimates of precipitation over a wide area.

4.6 Radar-estimate calibration by raingauge in view of Z-R relationship modification and appropriate correspondence between calibration targets

Detailed procedures for deriving Radar-AMeDAS precipitation have been described by Forecast Division (1991). This section outlines an algorithm that was developed in June 1995 to improve fields for calibrating radar precipitation over land areas.

Although radar estimates are improved with the algorithm in Section 4.5, more reliable estimates are obtained on land, or areas where there is a raingauge within a 70-km in radius, by a correction method using AMeDAS raingauge data.

In this algorithm, a value of Radar-AMeDAS precipitation at a pixel g, R_g, is described with a calibration factor, F_g, as follows:

$$R_g = F_g E_g \tag{4.6.1}$$

where E_g denotes the radar-precipitation amount.

The calibration factor F_g is described with the calibration factors F_i derived from comparison between a raingauge measurement and the corresponding radar precipitation, as follows:

$$F_g = \exp\left(\sum_i (\ln F_i) W_i / \sum_i W_i\right) \tag{4.6.2}$$

where W_i is the weight on F_i for interpolation.

At the second and the third repetition of the successive modification processes, radar precipitation amount E_g, in Eq. (4.6.1) is replaced by R_g determined with Eq. (4.6.2) in the former process.

4.6.1 Weight for interpolation considering precipitation intensity

Weight for interpolation, W_i, includes a factor for the difference between the radar precipitation at the target pixel g and that at the pixel where AMeDAS raingauge i is located, as well as a factor for the distance between

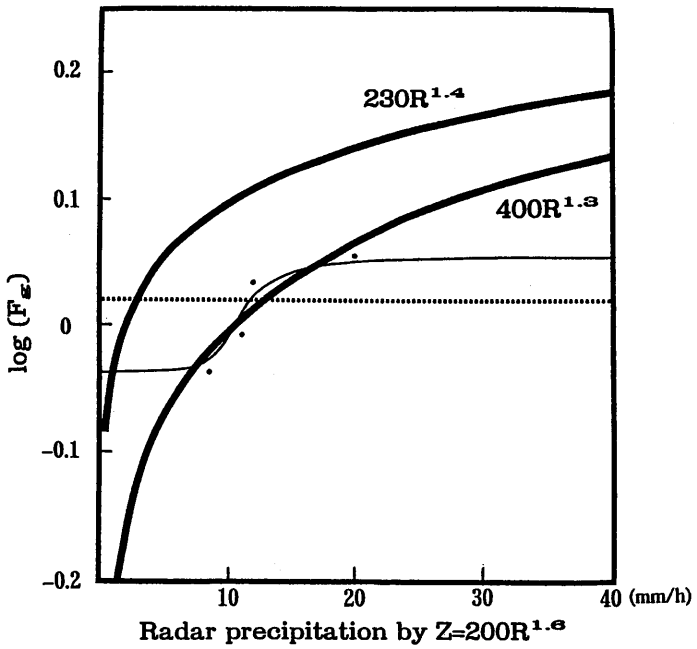

Fig. 4.6.1 Approximations with different algorithms to the observed calibration factors which change depending on the local variability of precipitation intensity. The horizontal axis indicates the precipitation rate by a Z-R relationship, $Z=200R^{1.6}$, and the vertical axis denotes the calibration factor, that is the rate of the actual precipitation to the radar estimate by the standard Z-R relationship in a logarithm scale. Dots in the figure indicate calibration factors calculated by actually comparing radar data with raingauge data. The broken line is produced by interpolating those calibration factors concerning only distance. The solid thin line is produced by interpolation considering distance and precipitation intensity. Solid thick lines are calibration factors derived for different Z-R relationship values, that is the ratio of precipitation estimated with different B and β to that with the standard Z-R relationship for the same reflectivity factor Z. Variations for solid thick lines are from Austin (1987).

them, as the following equation indicates:

$$W_i = \frac{\exp(-d^2/D^2)}{1+a(E_g/E_i-1)^2}P_i \tag{4.6.3}$$

where

d: distance between Pixel g and the pixel where Raingauge i is located,

E_g: radar precipitation at Pixel g,

E_i: radar precipitation at the pixel where Raingauge i is located,

P_i: weight based on the reliability of AMeDAS data and radar data at the pixel where Raingauge i is located,

D,a: parameters.

By interpolating F_i with W_i, F_g's are different according to the precipitation rate of the pixel. Parameters D and a change according to the cycles of the successive modification. In the first cycle, D and a are large, in order that W_i may be determined mainly by the difference of precipitation intensity. In the later cycles, D and a are set smaller for calibrating the precipitation the rate of which changes depending mainly on the location.

Figure 4.6.1 compares this effect with other algorithms. The dots indicated in the figure denote the calibration factors calculated over the respective raingauges. Methods to change B and β correspond to solid thick lines. These solid curves are determined by fixing the two parameters so that the total difference between the values of the curve and the values indicated by dots may be the minimum. Interpolation only about the distance

(Makihara et al., 1995) changes its calibration factor with no relation to the precipitation rate, as described by the broken line. The curve which the algorithm in this section describes changes according to the weight on the intensity of radar precipitation over the dots. The difference between this algorithm and changing of B and β is clear at high intensity which is not observed with raingauges. The curve determined by fixing B and β sometimes indicates larger factors for extremely strong rainfall, while the current algorithm's values seldom exceed observed ones. The current algorithm can avoid yielding excessive factors for strong reflections from very large raindrops or even from large particles of hails.

The weight P_i based on the reliability of observation data becomes smaller when:

1) An AMeDAS raingauge or a radar observes very light precipitation, where an error caused by digitization may occur
2) The altitude at which a radar observes precipitation echo is high
3) The number of AMeDAS raingauges for determining F_g is small.

4.6.2 Correspondence between raingauge measurement and radar precipitation

In determining F_i, it should be taken into account that an AMeDAS measurement does not always correspond to the radar precipitation of the same pixel of 5 km square, because 1) there is variability in the distribution of precipitation even in a 5-km pixel, and 2) raindrops aloft are often carried away to another pixel before they reach the ground. Unsuitable correspondence between an AMeDAS measurement and a radar precipitation leads to a false calibration factor. To avoid this undesirable situation, we use the following process, taking into account the eight pixels surrounding the target pixel:

$$F_i = f(C_c, C_s, C_l, C_v, N) \tag{4.6.4}$$

where

C_c: (AMeDAS measurement, R)/(radar precipitation of the target pixel, E_i),

C_s: R/(maximum radar precipitation among the pixels, E_l),

C_l: R/(minimum radar precipitation among the pixels, E_s),

C_v: R/(average of radar precipitation estimates of the pixels),

N: number of AMeDAS raingauges concerning the calculation of F_g over the target pixel.

In the process, C_c is used as F_i when $|C_c|$ does not exceed the value of Parameter γ, while other values are taken into account when $|C_c|$ exceeds γ, considering that a large $|C_c|$ may be due to unsuitable correspondence. For example, when C_c exceeds γ, F_i is determined by the following equation:

$$F_i = \min(\max(1, C_v\delta), \max(\delta, \min(3, \max(1, 0.5N))C_s), C_c) \tag{4.6.5}$$

where min and max indicate the minimum and the maximum among the values within parentheses, respectively, and δ is a constant. Almost the same restriction is placed on C_c below $-\gamma$.

Figure 4.6.2 illustrates this function. In the figure, F_i is equal to C_c if C_c is in the hatched area, while F_i changes to the value at the top of the hatched area if C_c exceeds the area. The adoption of the new value is equivalent to making the raingauge measurement correspond with the radar precipitation of the intensity between E_i and E_l for obtaining a smaller calibration factor. It is also found by the figure that the function imposes severe restriction when the target has a small number of AMeDAS sites concerned.

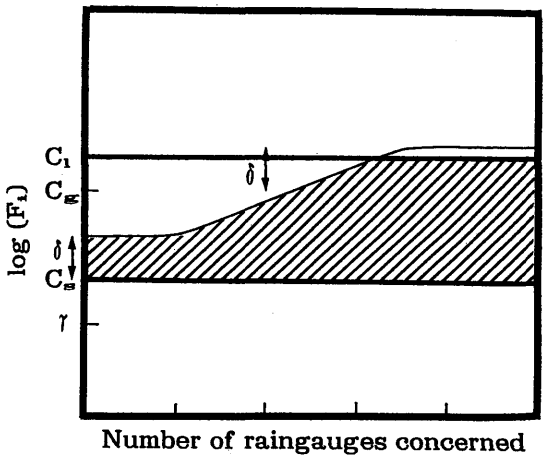

Fig. 4.6.2 Schematic diagram showing how to correspond an AMeDAS measurement with the radar observations at the target and surrounding pixels. The figure illustrates the case when the calibration factor between the AMeDAS measurement and the radar observation over the target pixel exceeds a criterion value γ. Hatched area shows the range where F_i can be allowed.

Consequently, this function makes an AMeDAS raingauge measurement correspond to a radar precipitation so that 1) Radar-AMeDAS may be equal to the AMeDAS measurement if $|C_c|$ is under γ, and 2) Radar-AMeDAS may be close to the radar precipitation with small modification by AMeDAS under the restriction of Eq. (4.6.5) in other cases.

4.7 Accuracy of Radar-AMeDAS precipitation

4.7.1 Introduction

Radar-AMeDAS precipitation, Radar-AMeDAS hereafter provides important information for warnings and watches for heavy rainfall issued by JMA, because of its detailed continuous distribution of precipitation. Several reports were presented concerning the accuracy of Radar-AMeDAS on land (e.g. Nyoumura, 1985, Kitabatake et al., 1991). However, since the algorithm for Radar-AMeDAS has been improved over the past several years, we will clarify the effect of the new algorithms in this study.

The accuracy over the sea cannot be verified with raingauge, and should be estimated indirectly by other means. As one of those means, we prepare a distribution of appearance frequencies of Radar-AMeDAS pixels for different intensities, and compare it with that of AMeDAS.

4.7.2 Data

The target of verification in this study is values of 1-hour precipitation amount of Radar-AMeDAS for pixels of 5-km square, which are allocated onto a composite domain shown in Fig. 4.3.1. Operational products of Radar-AMeDAS after March 1993 are used for most of the verifications. Products re-analyzed by the algorithm that has been operational since June 1995 are also used for the cases before March 1993.

A very dense raingauge network of the Tokyo Metropolitan Government with average spacing of 4.5 km is used for detailed comparison, and raingauge data from other local governments and from the Ministry of Construction are used for verifying severe rainfall over 100 mm/h. None of those data was used in Radar-

AMeDAS analysis.

For obtaining Radar-AMeDAS, data from JMA conventional radars and AMeDAS raingauges are used.

An estimate of 1-hour precipitation by radar, radar precipitation hereafter, is derived from the reflectivity factor Z observed on a 2.5 km grid by using a Z-R relationship of 200 for B and 1.6 for β (Marshall and Palmer, 1948).

The grid size for radar precipitation is changed from 2.5 km to 5 km before the data are transmitted to the JMA forecast center by choosing the maximum value among four pixels of 2.5 km square.

4.7.3 Representative precipitation for a 5-km square pixel

Radar-AMeDAS should have the following features as a representative value of precipitation for a pixel of 5 km square:

1) It should not fail to detect local severe precipitation.
2) It should be "more accurate" with the help of AMeDAS raingauge data than radar precipitation.

Before verification, we consider the representative value of Radar-AMeDAS because severe precipitation cells such as from thunderstorms sometimes have a large areal variation even in an area of 5-km square.

Owing to the variability in the Z-R relationship or the vertical difference of reflectivity from radar precipitation, precipitation needs calibration to achieve sufficient accuracy (Collier et al., 1975). Since measurements of precipitation at AMeDAS raingauges are considered to be random sampling from the actual precipitation distribution, AMeDAS can be assumed to represent the average of precipitation in a 5-km square when statistically processed on both space and time. Therefore, calibration with AMeDAS is expected to produce, in general, Radar-AMeDAS representing the average value in a 5-km square. Here, it should be noted that calibration with AMeDAS includes not only improvement in accuracy of radar precipitation but also modification of the representative radar precipitation for a 5-km square into the average.

The representative value of radar precipitation for a 5-km square, that is the maximum of four radar precipitation measurements in a 2.5-km square, represents more localized severe precipitation suitable for real-time watching tasked for Radar-AMeDAS.

Under these circumstances, the following two extreme cases of calibration are possible:

1) When scarcely calibrated, Radar-AMeDAS represents almost the maximum among four 2.5-km pixel values in a 5-km pixel.
2) When calibration with AMeDAS is heavily imposed, Radar-AMeDAS becomes statistically the average precipitation in a 5-km pixel.

For example, let a 5-km pixel consist of three 2.5-km pixels of 4 mm/h and one pixel of 20 mm/h, and these radar precipitation estimates be accurate. If there are many AMeDAS raingauges and 5-km pixels with the same condition, the most probable situation is that these AMeDAS raingauges measure values of 4 mm and 20 mm at a frequency rate of three to one. When we adopt calibration in case 2), Radar-AMeDAS becomes the average of 8 mm, while the case 1) provides 20 mm for Radar-AMeDAS. It should be noted that 8 mm from case 2) is the correct value for the areal average precipitation in a 5-km pixel and that 20 mm by case 1) is better for real time watching for severe precipitation.

The current algorithm arranges both cases depending on the conditions. For localized severe precipitation, case 1) is dominant. In this situation, the algorithm makes an AMeDAS measurement correspond to the radar

precipitation having as small modification factor as possible among the surrounding pixels, taking into account the location errors and large variability in a 5-km pixel (Section 4.6.2). For the other types of precipitation, the representative value of Radar-AMeDAS is close to one in case 2). There, radar precipitation representing the maximum of four 2.5-km pixels is modified with some nearby AMeDAS measurements into almost the average of the 5-km pixel. Variation in precipitation estimates of nearby pixels and the number of AMeDAS raingauges used for the calibration of the target pixel are, fundamentally, the parameters for determining how the weights should be distributed to those cases.

As the result, Radar-AMeDAS represents the following values:

1) For a precipitation with large variation often observed in a severe convective cells, Radar-AMeDAS represents the maximum of four 2.5-km pixels in each 5-km pixel
2) For a large scale precipitation with small variation in distribution, Radar-AMeDAS represents the value close to the average of precipitation in a 5-km pixel

Although less calibration is made in case 1) than in case 2), calibration on a larger scale is conducted for the entire detection area, beforehand, for both cases using data from all of the AMeDAS stations concerned (Section 4.5).

4.7.4 Detailed accuracy on land evaluated with raingauge data

To assess the accuracy of Radar-AMeDAS in detail, we compare Radar-AMeDAS with raingauge data except AMeDAS. In the comparison, a location error of one pixel (i.e. 5 km) must be taken into account because raindrops are sometimes advected by wind before reaching the ground, and there is also a possibility of an error reaching one pixel when Radar-AMeDAS values analyzed for respective radars are allocated onto the composite domain.

Raingauge data from the Tokyo Metropolitan Government is suitable for this comparison. In Fig. 4.7.1, these raingauge measurements are indicated on Radar AMeDAS chart at 6 JST on 9 October 1992, when an extratropical depression passed over. It is seen that Radar-AMeDAS values show good agreement with these raingauge measurements.

Figure 4.7.2 shows a case of a severe local thunderstorm at 22 JST on 20 May 1992. A large variation in precipitation distribution is seen even in a 5-km pixel. For example, in the pixel where Radar-AMeDAS indicated 39 mm, a raingauge measured 32 mm in its top left side and another gauge indicated only 6 mm in its bottom right side. Although in the pixel where AMeDAS measured 5 mm Radar-AMeDAS showed a rather larger value of 30 mm, and a raingauge in the next pixel on the right side measured 29 mm. Thus, with a location error of one pixel considered, Radar-AMeDAS provides good agreement. It is noteworthy that Radar -AMeDAS agrees with the largest raingauge measurement in a pixel in this case.

Figure 4.7.3 is a scatter diagram for comparisons between hourly Radar-AMeDAS values and corresponding raingauge measurements of the Tokyo Metropolitan Government for 4 months. A raingauge measurement was compared with the value that showed the best agreement among the grid containing the gauge site and the eight surrounding grids. Good agreement is seen also in this figure.

In Table 4.7.1, severe rainfalls that measured over 100 mm/h with raingauges are compared. Most of the radar data for these cases are obtained at a further distance from radars than the data for the verifications of the Tokyo area. Half of these cases are within an error of 15 %. The cases with relatively large-scale distur-

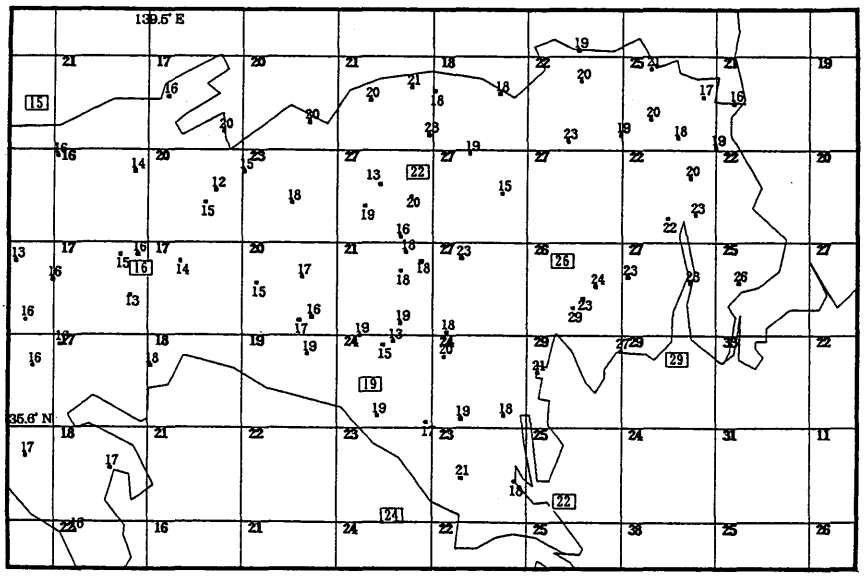

Fig. 4.7.1 Comparison of Radar-AMeDAS values with raingauge measurements of the network of the Tokyo Metropolitan Government at 6 JST on 9 October 1992. Radar-AMeDAS values and raingauge measurements are indicated by a numeral over the chart for a case when an extratropical depression passed over. The size of each pixel is the same as in Fig. 4.2.2, i.e. almost 5 km by 5 km. Points with numbers indicate locations of raingauges, and the numbers for each point denote the precipitation measured there. Numbers surrounded by a rectangle indicate raingauge readings by AMeDAS. The exact location of the AMeDAS site is on the vertex of the bottom left side. The Radar-AMeDAS value for each pixel is indicated in its top left side. It is seen that Radar-AMeDAS values agrees well with the raingauge measurements.

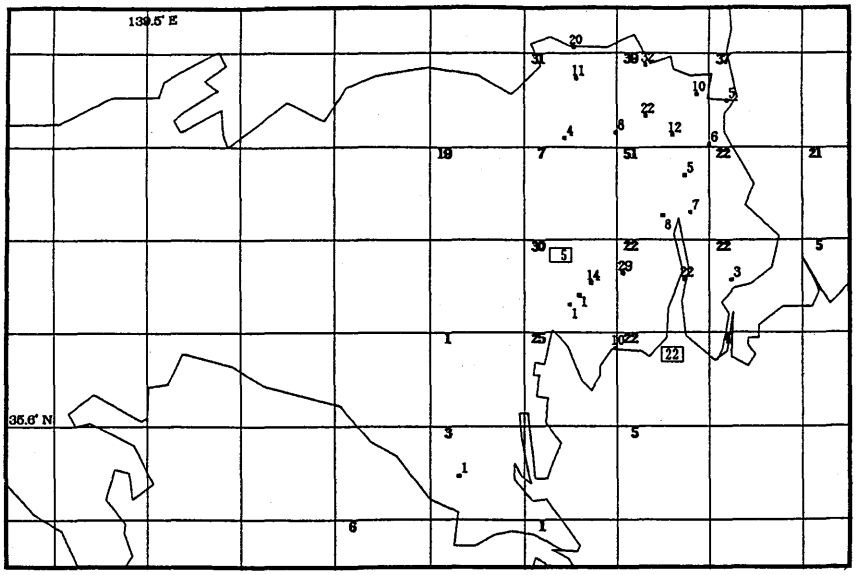

Fig. 4.7.2 Same as Fig. 4.7.1 except for the case of a thunderstorm at 22 JST on May 1992. There is a large variation in intensity even in a pixel. In the pixel where AMeDAS indicates 5 mm, Radar-AMeDAS value shows a larger value of 30 mm. However, a raingauge in the next pixel on the right side measures 29 mm. It should be noted that Radar-AMeDAS agrees with the largest raingauge measurement in the pixel in this case.

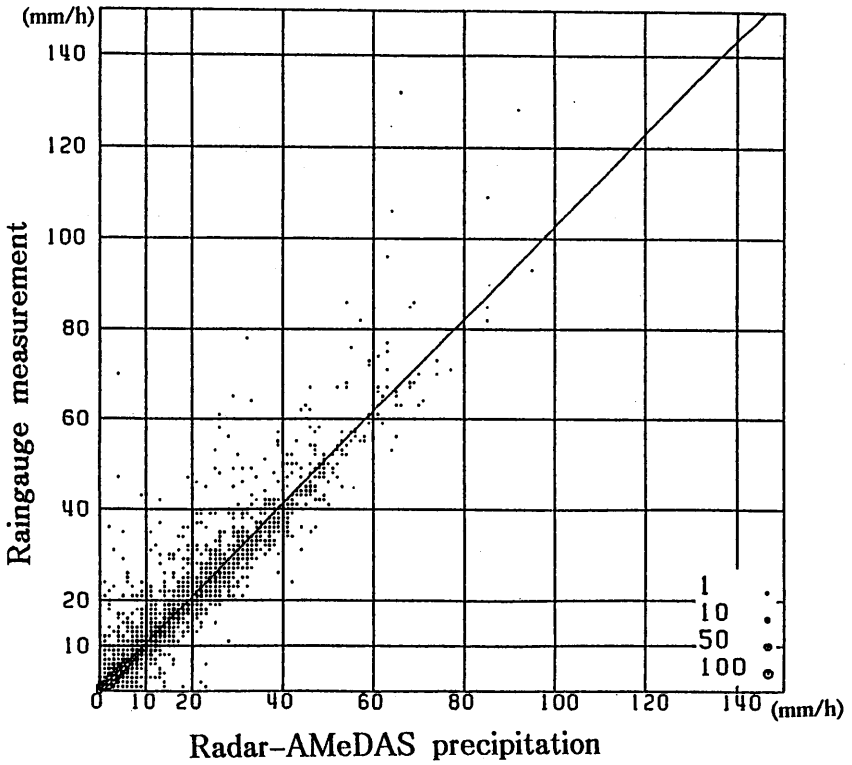

Fig. 4.7.3 Scatter diagram for comparisons between hourly Radar-AMeDAS values and raingauge measurements of the Tokyo Metropolitan Government for 4 months. Data from May to September in 1994, that is 5,808 cases, are used. A raingauge measurement is compared to the value which showed the best agreement among the pixel including the gauge site and the surrounding eight pixels. The figure looks as if Radar-AMeDAS values are slightly underestimated compared to raingauge measurements. This apparent underestimation is mainly due to the way of correspondence between a raingauge measurement and a Radar-AMeDAS value. The figure indicates only whether raingauge measurements can be detected by Radar-AMeDAS with sufficient accuracy.

bances are estimated within an error of 30 %. The rest includes three cases with an error of about 40 % to 50 % and one case of 70 %, all of which are brought about by localized convection. The last worst case was greatly affected by attenuation of the radar beam due to a film of water over a radome produced by severe rainfall.

This evaluation indicates only whether Radar-AMeDAS unfailingly detected such severe precipitation amounts because those raingauge data are only part of the entire severe precipitation amounts. To determine the accuracy of Radar-AMeDAS, we also have to know at the same time, how few the overestimates are among all of the Radar-AMeDAS values. However, it is almost impossible to verify all of severe Radar-AMeDAS values having spatial continuity by using scattered raingauges. Another approach is necessary for this kind of verification.

4.7.5 Comparison by appearance rates

The density of a raingauge network is, in general, not so high as to correspond with every pixel of Radar-AMeDAS. Here, by comparing frequencies of the appearance for different intensities, all Radar-AMeDAS values will be evaluated statistically with AMeDAS.

The distribution of the frequencies of raingauge measurements for different intensities is known, in general, to exhibit a gamma distribution (for example Suda, 1993). If the number of AMeDAS raingauges increased to the spacing of 5 km, the observation frequencies would increase. In this case, the increase of observation

Table 4.7.1 Raingauge data for extremely severe rainfall and corresponding Radar-AMeDAS values

Data and time (JST)	Location (Prefecture)	Raingauge Value (mm/h)	Radar-AMeDAS (mm/h)	Situation	
1993. 6.21.15	Tokyo	112	59	Thunderstorm	H
1993. 8. 1.20	Kagoshima	119	105	Rain band	
1993. 9. 3.16	Kagoshima	116	100	Typhoon	OH
1993.11.13.10	Tokushima	115	120	Depression	OH
1993.11.13.10	Tokushima	110	140	Depression	OH
1993.11.13.10	Tokushima	107	105	Depression	OH
1993.11.13.10	Tokushima	105	130	Depression	OH
1994. 9. 7. 0	Osaka	106	64	Local convection	
1994. 9. 7. 1	Osaka	108	110	Local convection	
1994. 9.22.13	Miyagi	132	66	Thunder storm	
1994. 9.22.15	Miyagi	134	43	Thunder storm	H
1994. 9.22.16	Miyagi	121	130	Thunder storm	H

Note: Marks "O" and "H" at the last of each case indicate existence of orographic effect and high calibration factor required, respectively.

frequency for each intensity is expected to be proportional to the increase of raingauges because the condition for sampling the actual precipitation with AMeDAS raingauges does not change except for the sampling number. As a result, "the ratio of the number of measurements for specific intensity to the total number of measurements including 0" is not influenced by their spatial density. Hence, by using this ratio, the frequency distribution of Radar-AMeDAS composed of 5-km pixels can be evaluated on land with the same condition as that of AMeDAS.

On the other hand, there may be some difference between the actual distribution over the sea and that over land. Almost the same distribution is expected, however, since the period during which those distributions were collected has a duration of over 3 months, and the target domain is so large that the sea area can be treated as being near the land, although some difference may be found in areas affected by orography. In fact, the appearance frequencies of radar precipitation for the land area and for the sea area which are normalized with respect to the total number of pixels show only a small difference for each intensity as shown in Fig. 4.7.6.

With those considerations in mind, the appearance rate of Radar-AMeDAS is compared with that of AMeDAS for the land area and for the sea area, as well as for a warm season and for a cold season, respectively.

In addition, verifications are made also for the different heights at which radars observe precipitation echoes. Some studies pointed out that the intensity of radar precipitation decreases as the observation height increases owing to the variable vertical profile of a rainfall echo (Joss et al., 1989; Joss, 1990). Although the algorithm of Radar-AMeDAS compensates for this effect as described in Section 4.5 to a certain extent, the compensation is insufficient in extreme cases such as for an area where a radar observes almost the top of rainfall. The relationship between these heights and the appearance rate is also investigated in the same manner.

4.7.5.1 Method

The number of pixels in which Radar-AMeDAS showed specific intensity are accumulated for different intensities and heights at which a radar observes precipitation echoes. Data from June to September 1993 are accumulated as those of a warm season, and data from December 1993 to February 1994 as of a cold season. Since the total numbers of pixels including no precipitation are different if the observation heights or the regions are different, we calculate "an appearance rate," f, by normalizing with respect to the total number of

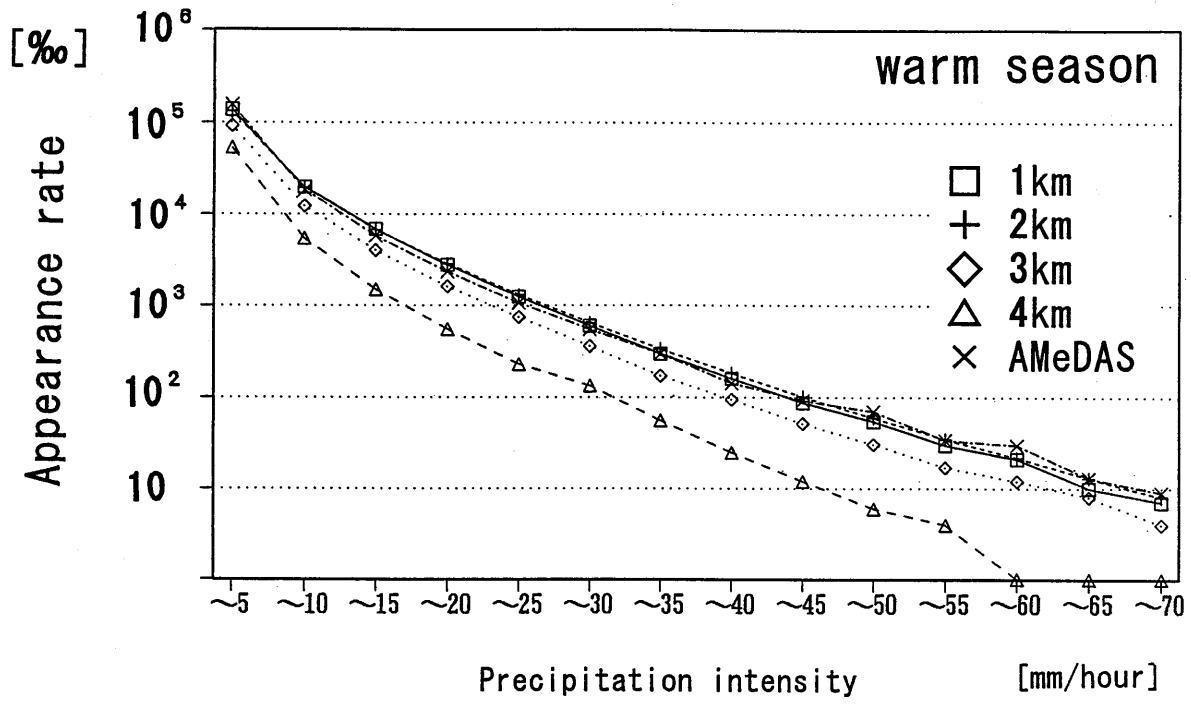

Fig. 4.7.4 Appearance rates of Radar-AMeDAS values for different observation heights. The horizontal axis denotes precipitation intensity in mm/h, and the vertical axis indicates the appearance rate. The rate at a specific intensity indicates the ratio of the number of pixels where Radar-AMeDAS values of the specific intensity are observed to the total number of all the pixels. The rates are expressed as common logarithms of PPM, $\log(1{,}000{,}000 N_{echo}/N_{pixcel})$. Data from June to September in 1993 were used. The rate of Radar-AMeDAS values at observation height of 2 km and under is almost identical to that of AMeDAS measurements.

frequencies as follows:

$$f(h,r) = s(h,r) / \sum_{r=0}^{\infty} s(h,r) \tag{4.7.1}$$

where

h: height at which a radar observes a precipitation echo

r: precipitation intensity

s: frequency at Intensity r and at Observation height h.

4.7.5.2 Results

For determining the relationship with observation heights, the appearance rates of Radar-AMeDAS for the warm season are shown in Fig. 4.7.4 together with that of AMeDAS. The appearance rate of Radar-AMeDAS at observation heights of 2 km or less shows fairly good agreement with that of AMeDAS. The appearance rate at 3 km is smaller than that of AMeDAS by about 60 % for all intensities.

The appearance rates in the cold season show similar differences as in the warm season (Fig. 4.7.5). The higher rate of AMeDAS in weak precipitation might be caused by precipitation with a low cloud top height which cannot be detected by radar in spite that raingauges can detect one.

We, then, evaluate the difference in the appearance rate in terms of intensity, to obtain a standard for estimating areal precipitation amounts. It is assumed that the appearance rate of AMeDAS is equivalent to the actual rate. It is also assumed that the intensity of Radar-AMeDAS values can be described as a function which

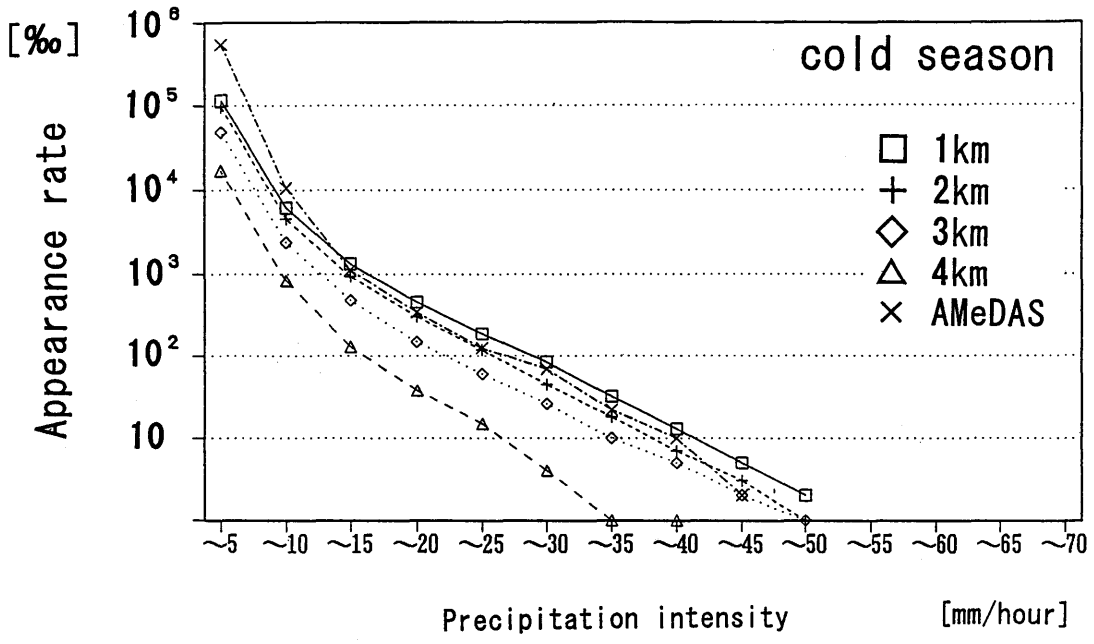

Fig. 4.7.5 Same as Fig. 4.7.4 except for the period from December 1993 to February 1994.

increases monotonically with the increase of the intensity of AMeDAS, although the relationship may not be proportional.

We can then determine the value of Radar-AMeDAS, R', so that the sum of the appearance rates of Radar-AMeDAS from infinity to R' may be the same as that of AMeDAS from infinity to R, as follows:

$$\sum_{r=R}^{\infty} f_a(r) = \sum_{r=R'}^{\infty} f(h,r)$$

Where

f_a: appearance rate of AMeDAS

The concept and the assumption of this method are similar to what Rosenfeld et al. (1993) proposed for deriving the relation between radar-precipitation amounts and raingauge measurements for different types of precipitation events, although the purpose and the applied data are different.

Under the above assumption, the actual intensity of the precipitation which Radar-AMeDAS analyzed as R' is considered to be R. Consequently, R'/R is the ratio of the intensity of Radar-AMeDAS to that of the actual precipitation. The result obtained by this method indicates that Radar-AMeDAS at 3 km underestimates the intensity by 20 % at 20 mm/h, and 28 % at 50 mm/h over the sea (Fig. 4.7.7). The small values at low intensity around 5 mm/h over the sea are mainly due to failing in detection of precipitation, which disagrees with the assumption on Eq. (4.7.2).

For detailed evaluation of the appearance rates at lower observation heights, the ratios of the appearance rate of Radar-AMeDAS to that of AMeDAS in the warm season are shown in Fig. 4.7.6 both for the land and for the sea respectively. The ratio for radar precipitation, which is not calibrated with AMeDAS, is also included in the figure. Figure 4.7.6 shows that the ratio of the radar precipitation is smaller than that of AMeDAS, especially at high intensity. Since Radar-AMeDAS shows the ratio much closer to 1 than radar precipitation,

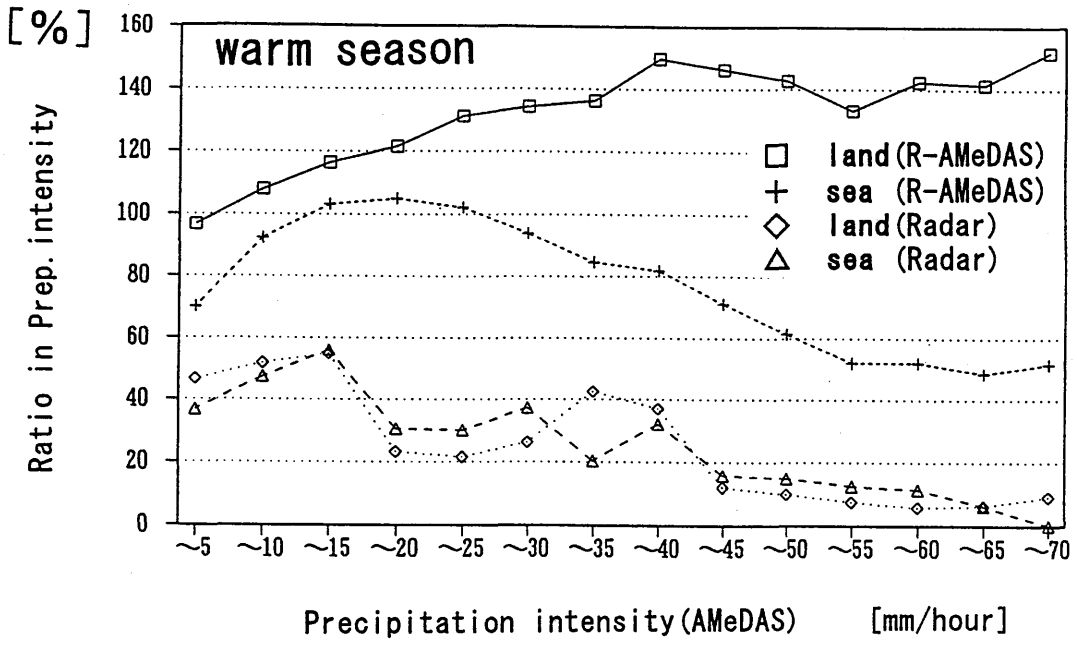

Fig. 4.7.6 Comparison of the appearance rates of Radar-AMeDAS values over the land and over the sea with that of AMeDAS. Ratios of the appearance rates of Radar-AMeDAS values to those of AMeDAS in the warm season are shown for the land and for the sea, respectively. The ratios for radar precipitation, which is not calibrated with AMeDAS, are also included.

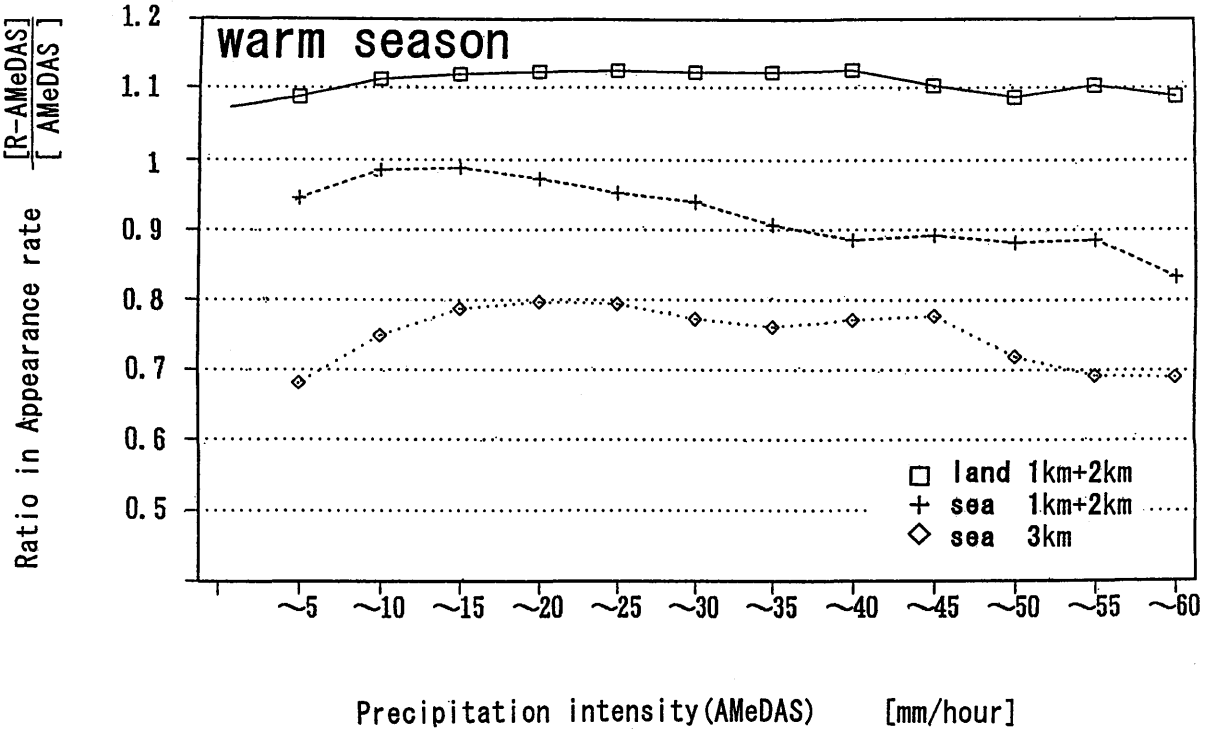

Fig. 4.7.7 Evaluation of Radar-AMeDAS about intensity for estimating areal precipitation amounts. The ratio of intensity that Radar-AMeDAS indicates to the actual intensity is shown under the assumption that the appearance rate by AMeDAS is equal to the actual one. It should be noted that Radar-AMeDAS not only seeks to determine accurate areal precipitation but also must always detect localized severe precipitation. The positive bias over the land area is caused mainly by this task. Since the figure is indicated by the ratio, the values at higher intensity are relatively close to 1 in spite of the larger differences in their appearance rates.

it is clear that the performance of Radar-AMeDAS surpasses that of radar precipitation.

The ratios of Radar-AMeDAS for the land area exceed 1 for all intensities, and they become larger as the intensity increases. This feature is consistent with the result from the consideration on the representative value for a 5-km pixel in Section. 4.7.3. In estimating areal rainfall amounts, Radar-AMeDAS overestimates AMeDAS by 11 % at 10 mm/h and by 12 % at 40 mm/h although overestimation decreases to 8 % at 5 mm/h (Fig. 4.7.7).

On the other hand, the ratio over the sea is very similar to that of AMeDAS at low intensity, while it decreases at high intensity over 15 mm/h. When Eq. (4.7.2) is applied, Radar-AMeDAS over the sea gives underestimation of the intensity by 2 % at 10 mm/h, and 12 % at 40 mm/h under the assumption that the appearance rate of AMeDAS is equal to that over the sea. Since the appearance rates around 40 mm/h are 1/100 to 1/1,000 of that at 5 mm/h, the effect of the errors in this intensity on the total areal precipitation over an area is expected to be under 1 %.

The following are major reasons accounting for the decrease at high intensity.

1) Local calibration by AMeDAS is not available for Radar-AMeDAS over the sea. The Z-R relationship used for the JMA radars is thought to cause underestimation at high intensity for local convections (Fujiwara 1965). The underestimation caused by vertical difference of precipitation intensity is also, in general, larger for the area with higher intensity than the areas with lower intensity surrounding it. These are considered to lead to the underestimation of the actual intensity at higher intensities.
2) Orographic effect is less prominent over the sea. This leads to fewer occurrences of severe precipitation over the sea than over the land.

   As for the severe rainfall events in Table 4.7.2, five of them are considered to be affected by orography, and the three remaining had large calibration factors. If those events had occurred over the sea, the five events would have lower rainfall intensities, which would lead to smaller appearance rates at high intensity. The three remaining would be estimated to have smaller intensities with smaller calibration factors because of no local calibration. It is difficult to estimate only with those figures, however, the orographic effect might not be small enough to be neglected in evaluating Radar-AMeDAS over the sea with AMeDAS.

4.7.6 Conclusions

The very dense raingauge network of the Tokyo Metropolitan Government was used for the detailed evaluation of Radar-AMeDAS. By evaluating Radar-AMeDAS for a pixel of 5 km square with several raingauges located in the pixel, it was found that Radar-AMeDAS represents almost the average of those raingauge measurements when precipitation is caused by a large scale disturbance, and that it is close to the maximum raingauge measurement in the pixel when the precipitation is as localized as scattered thunderstorms. In a comparison over a period of approximately 4 months, Radar-AMeDAS exhibited an excellent agreement if a positioning error of one pixel was allowed.

Radar-AMeDAS values were also compared with AMeDAS raingauge measurements and with radar-precipitation amounts statistically, with respect to the appearance rates, for different precipitation intensities. The comparison revealed that Radar-AMeDAS is much more accurate than radar precipitation, which is determined only with constant Z-R relationship and shows small appearance rates. The rate of Radar-AMeDAS agrees well with that of AMeDAS if radar observation is made at an altitude below 3 km. For radar observation at

3 km height, the appearance rate decreases to about 60 % that at 2 km height. Under the assumption that AMeDAS represents the actual appearance rate, this rate is equivalent to underestimation of areal precipitation amounts by 20 % at 20 mm/h and 28 % at 50 mm/h.

Since Radar-AMeDAS precipitation on land sometimes represents the maximum of precipitation in a pixel for the purpose of unfailingly detecting extremely localized severe precipitation, it exhibits higher appearance rates at higher precipitation rates than AMeDAS. As a result, in estimating areal rainfall amounts, Radar-AMeDAS overestimates AMeDAS by 11 % at 10 mm/h and 12 % at 40 mm/h, although overestimation decreases to 8 % at 5 mm/h.

Radar-AMeDAS over the sea, where there is no local calibration by AMeDAS and little influence of orography, exhibits smaller appearance rates over 15 mm/h than AMeDAS at 10 mm/h in intensity and 12 % at 40 mm/h. This smaller appearance at high intensity is mainly caused by the followings.

1) A Z-R relationship sometimes unsuitable for convective severe rainfalls, and a vertical precipitation profile with characteristic leading to large underestimation at high intensity are major targets which should be calibrated on a local scale. These cannot be calibrated on a local scale without AMeDAS.
2) The occurrences of the events of high intensity are fewer due to smaller orographical effect over the sea than over the land

   Because of the effects in 2) the actual underestimation of Radar-AMeDAS over the sea is thought to be smaller than the values in Fig. 4.7.7. In addition, when only a total areal amount for a rather large area is considered, the influence of underestimation at high intensity might be quite small because appearance rates at high intensity (around 40 mm/h) are much smaller than those at lower intensity (around 5 mm/h).

Appendix (1)

In this appendix, all the variables are the same as those in Section 4.5.4.3.1, and it is assumed that X_b^* makes J_{2a} the minimum among three candidates, and $X_b^* - \Delta$ the second smallest.

The following are some situations when weighting coefficients ε, ξ, η are determined.

1) When the difference between $J_{2a}(X_b^*-\Delta)$ and $J_{2a}(X_b^*)$ is large, X_b should be close to X_b^* in order to keep J_{2a} small, which leads to large weighting of ξ and η. On the other hand, when there is little difference between $J_{2a}(X_b^*-\Delta)$ and $J_{2a}(X_b^*)$, the increase in J_{2a} is small as long as X_b is almost between $X_b^*-\Delta$ and $X_b^* + \Delta$, and X_a satisfies Eq. (4.5.15). Therefore, it is more effective to put larger weighting to ε than to others, in order that J_2 for Radar b and radars other than a may be small.
2) If $J_{2a}(X_b^*)$ is large, there are two possibilities: (1) X_b^* is not proper, or (2) the assumption in Eq. (4.5.15) has some errors. In this case, in order to avoid false modification of these parameters, smaller weighting is given to the three coefficients. This treatment makes the influence of L_2 for these radars on the total L_2 in Eq. (4.5.17) small in the early stage of the iteration.
3) When all the data for Radar b are of the same beam height, J_{2a} can be resolved only when corresponding heights of Radar a show different values. Actually, Eq. (4.5.11) can be transformed as follows because B_{bk} is independent of point k:

$$J_2(X_a, X_b) = K\frac{\sum_k (a_{ak}/E_{bk})^2}{\{\sum_k (a_{ak}/E_{bk})\}^2} - 1 + K\frac{\sum_k (E_{bk}/a_{ak})^2}{\{\sum_k (E_{bk}/a_{ak})\}^2} - 1$$

This equation does not include X_b. Hence, C_{ab} becomes zero, and X_b^* cannot be determined in this case. Here, when all the data for Radar b are of nearly the same beam height, the reliability of X_b^* must be low, even if they may be derived. In this case, the coefficient C_{ab} may be small, and differences among J_2's for three occasions may also be small.

In the same way, when all of the beam height values of Radar a are almost the same, the reliability of X_a^* is small, and the coefficient C_{ab} is large, although the coefficients may be derived.

With these considerations, the actual weighting is determined. Specific values for the coefficients used in this study are as follows:

(a)

$$\varepsilon = W_1,$$
$$\varsigma = W_1 W_2,$$
$$\eta = 0.5 W_1 W_2,$$
$$W_1 = 1/J_{2a}(X_b^*),$$
$$W_2 = \{0.25 + (J_{2a}(X_b^* - \Delta) - J_{2a}(X_b^*))/J_{2a}(X_b^*)\},$$

were $1/W_1$ is limited between 0.1 and 1.0.

(b) When C is nearly 0 (smaller than 1/16), ξ is 1, while ε and η are 0.

(c) When C is over 16, η is 1/2, while ε and ξ are 0.

Appendix (2): Weighting strategy for determining As

Coefficients α and γ used in Eq. (4.5.19) are determined as follows.

(a) γ is set larger when Δ is derived from the readings of raingauges at the target time, than when derived from statistical values.

(b) α is fixed to zero when there is no area where the radar observations overlap.

When radar echoes are over the sea only, Δ is not obtained at the target time; the value based on the statistics for the last 240 hours is then adopted as its substitute.

When $\Sigma\beta_{abk}$ are actually calculated, weighting is applied to every point concerned such that the total weight for every altitude level sliced at 500-m intervals is the same, and the number of samples for a radar estimate less than 1 mm/h is restricted to half of that for the other intensities, so as not to place excessive weight on small intensities in the analysis for the logarithm.

References

Andrieu, H. and J. D. Creutin, 1991: Effect of the vertical profile of reflectivity on the rain rate assessment at ground level. Preprints 25th Conf. Radar Meteor., 832-835.

Aoyagi, J., 1983: A study on the MTI weather radar system for rejecting ground clutter. Papers in Meteor. Geophysics, 23 No. 4, 187-243.

Austin, P. M., 1987: Relation between measured radar reflectivity and surface rainfall. Mon. Wea. Rev., 115, 1053-1070.

Brandes, E. A., 1975: Optimizing rainfall estimates with the aid of radar. J. Appl. Meteor., 14, 1339-1345.

Collier, C. G., T. W. Harrold and C. A. Nicholass, 1975: A comparison of areal rainfall as measured by a raingauge-calibrated radar system and raingauge networks of various densities. Preprints, 16th Conf. Radar Meteor., 467-472.

Doviak, R. J. and D. S. Zrnic, 1984: Doppler Radar and Weather Observations. Academic Press., New York, 458pp.

Forecast Division, Forecast Department, 1991: Data processing in the system for very-short-range forecast of precipitation. Weather Service Bulletin, 58, 189-207 (in Japanese).

Fujiwara, M., 1965: Raindrops-size distribution from individual storms, J. Atmospheric Science, 22, 585-591.

Golden, J., Sarreals, D. and Toephfer, F., 1986: NEXRAD and algorithms part 1 and part 2. Preprints, 23rd Conf. Radar Meteor. Cloud Physics, Snowmass, Colorado, Sept, 83-90.

Gray, W. R., 1991: Vertical profile corrections based on EOF. Analysis of operational data. Preprints, 25th Conf. Radar Meteor., 821-823.

Joss, J. and A. Waldvogel, 1989: Precipitation estimates and vertical reflectivity profile corrections. Preprints, 24th Conf. Radar Meteor., 682-688.

Joss, J. and A. Pittini, 1991: The climatology of vertical profiles of radar reflectivity. Preprints, 25th Conf. Radar Meteor., 828-831.

Joss. J., 1990: Way of using, and correcting for errors in conventional radar reflectivity data. Weather Radar Networking, 190-199, Kluwer Academic Pub., Dordrecht, Netherlands.

Kitabatake, N. and M. Obayashi, 1991: A study comparing radar-AMeDAS precipitation chart with observed data of raingauge network of Tokyo metropolis, J. Meteor. Research, 43, 285-310.

Makihara, Y., N. Kitabatake and M. Obayashi, 1995: Recent developments in algorithms for the JMA nowcasting system. part 1, Geophysical Magazine Series 2,1, 171-204.

Makihara, Y., 1996: A method for improving radar estimates of precipitation by comparing data from radars and raingauges, J. Meteor. Soc. Japan, 74, 459-480.

Marshall, J. S. and W. M. Palmer, 1948: The Distribution of raindrops with size. J. Meteor., 5, 165-166.

Nyomura, Y., 1985: Verification of JMA's precipitation observation system using digitized radar and raingauges (AMeDAS) by local dense raingauges system of Tokyo Metropolis, J. Meteor. Research, 37, 1-12.

Rosenfeld, D., D. Atlas, and D. B. Wolff, 1993: General probability-matched relations between radar reflectivity and rain rate, J. Appl. Meteor., 32, 50-72.

Sakota, Y., 1990: Radar echo digitizing and disseminating system. Tenki, 37, 659-670 (in Japanese).

Sliga, T. A., and V. N. Bringi, 1976: Potential use of radar differential reflectivity measurements at orthogonal polarizations for measuring precipitation. J. Appl. Meteor., 15, 69-76.

Suda, Y., 1993: Comparison of probable precipitation amounts in warm years and cold years, Tenki, 40, 335-341.

Takase, K., Y. Takemura, K. Aonashi, N. Kitabatake, Y. Makihara and Y. Nyomura, 1988: Operational precipitation observation system in Japan Met. Agency. Tropical Rainfall Measurements (John S. Theon and Nobuyoshi Fugono eds.), A. Deepak Pub., 407-413.

Takemura, Y., K. Takase and Y. Makihara, 1984: Operational precipitation observation system using digitized radar and rain gauges. Proc, Nowcasting-II Symposium, Norrk ping, Sweden, e-7 Sept. 1984, ESA SP-208, 411-416.

Tatehira, R and T. Shimizu, 1978: Intensity measurement of precipitation echo superposed on ground clutter-a new automatic technique for ground clutter rejection-. Preprints, 18th Conf. Radar Meteor., 364-369.

気象研究所技術報告一覧表

第１号　バックグラウンド大気汚染の測定法の開発（地球規模大気汚染特別研究班，1978）
Development of Monitoring Techniques for Global Background Air Pollution. (MRI Special Research Group on Global Atmospheric Pollution, 1978)

第２号　主要活火山の地殻変動並びに地熱状態の調査研究（地震火山研究部，1979）
Investigation of Ground Movement and Geothermal State of Main Active Volcanoes in Japan. (Seismology and Volcanology Research Division, 1979)

第３号　筑波研究学園都市に新設された気象観測用鉄塔施設（花房龍男・藤谷徳之助・伴野　登・魚津　博，1979）
On the Meteorological Tower and Its Observational System at Tsukuba Science City. (T. Hanafusa, T. Fujitani, N. Banno, and H. Uozu, 1979)

第４号　海底地震常時観測システムの開発（地震火山研究部，1980）
Permanent Ocean－Bottom Seismograph Observation System. (Seismology and Volcanology Research Division, 1980)

第５号　本州南方海域水温図－400m（又は500m）深と1,000m深－（1934－1943年及び1954－1980年）（海洋研究部，1981）
Horizontal Distribution of Temperature in 400m (or 500m) and 1,000m Depth in Sea South of Honshu, Japan and Western－North Pacific Ocean from 1934 to 1943 and from 1954 to 1980. (Oceanographical Research Division, 1981)

第６号　成層圏オゾンの破壊につながる大気成分及び紫外日射の観測（高層物理研究部，1982）
Observations of the Atmospheric Constituents Related to the Stratospheric ozon Depletion and the Ultraviolet Radiation. (Upper Atmosphere Physics Research Division, 1982)

第７号　83型強震計の開発（地震火山研究部，1983）
Strong－Motion Seismograph Model 83 for the Japan Meteorological Agency Network. (Seismology and Volcanology Research Division, 1983)

第８号　大気中における雪片の融解現象に関する研究（物理気象研究部，1984）
The Study of Melting of Snowflakes in the Atmosphere. (Physical Meteorology Research Division, 1984)

第９号　御前崎南方沖における海底水圧観測（地震火山研究部・海洋研究部，1984）
Bottom Pressure Observation South off Omaezaki, Central Honsyu. (Seismology and Volcanology Research Division and Oceanographical Research Division, 1984)

第10号　日本付近の低気圧の統計（予報研究部，1984）
Statistics on Cyclones around Japan. (Forecast Research Division, 1984)

第11号　局地風と大気汚染質の輸送に関する研究（応用気象研究部，1984）
Observations and Numerical Experiments on Local Circulation and Medium－Range Transport of Air Pollutions. (Applied Meteorology Research Division, 1984)

第12号　火山活動監視手法に関する研究（地震火山研究部，1984）
Investigation on the Techniques for Volcanic Activity Surveillance. (Seismology and Volcanology Research Division, 1984)

第13号　気象研究所大気大循環モデルーⅠ（MRI・GCM－Ⅰ）（予報研究部，1984）

A Description of the MRI Atmospheric General Circulation Model (The MRI・GCM－Ⅰ). (Forecast Research Division, 1984)

第14号　台風の構造の変化と移動に関する研究－台風7916の一生－（台風研究部，1985)

A Study on the Changes of the Three - Dimensional Structure and the Movement Speed of the Typhoon through its Life Time. (Typhoon Research Division, 1985)

第15号　波浪推算モデルMRIとMRI－Ⅱの相互比較研究－計算結果図集－（海洋気象研究部，1985)

An Intercamparison Study between the Wave Models MRI and MRI－II －A Compilation of Results－. (Oceanographical Research Division, 1985)

第16号　地震予知に関する実験的及び理論的研究（地震火山研究部，1985)

Study on Earthquake Prediction by Geophysical Method. (Seismology and Volcanology Research Division, 1985)

第17号　北半球地上月平均気温偏差図（予報研究部，1986)

Maps of Monthly Mean Surface Temperature Anomalies over the Northern Hemisphere for 1891－1981. (Forecast Research Division, 1986)

第18号　中層大気の研究（高層物理研究部・気象衛星研究部・予報研究部・地磁気観測所，1986)

Studies of the Middle Atmosphere. (Upper Atmosphere Physics Research Division, Meteorological Satellite Research Division, Forecast Research Division, MRI and the Magnetic Observatory, 1986)

第19号　ドップラーレーダによる気象・海象の研究（気象衛星研究部・台風研究部・予報研究部・応用気象研究部・海洋研究部，1986)

Studies on Meteorological and Sea Surface Phenomena by Doppler Radar. (Meteorological Satellite Research Division, Typhoon Research Division, Forecast Research Division, Applied Meteorology Research Division, and Oceanographical Research Division, 1986)

第20号　気象研究所対流圏大気大循環モデル（MRI・GCM－Ⅰ）による12年間分の積分（予報研究部，1986)

Mean Statistics of the Tropospheric MRI・GCM－Ⅰbased on 12－year Integration. (Forecast Research Division, 1986)

第21号　宇宙線中間子強度1983－1986（高層物理研究部，1987)

Multi－Directional Cosmic Ray Meson Intensity 1983－1986. (Upper Atmosphere Physics Research Division, 1987)

第22号　静止気象衛星「ひまわり」画像の噴火噴煙データに基づく噴火活動の解析に関する研究（地震火山研究部，1987)

Study on Analysis of Volcanic Eruptions based on Eruption Cloud Image Data obtained by the Geostationary Meteorological satellite (GMS). (Seismology and Volcanology Research Division, 1987)

第23号　オホーツク海海洋気候図（篠原吉雄・四竈信行，1988)

Marine Climatological Atlas of the sea of Okhotsk. (Y. Shinohara and N. Shikama, 1988)

第24号　海洋大循環モデルを用いた風の応力異常に対する太平洋の応答実験（海洋研究部，1989)

Response Experiment of Pacific Ocean to Anomalous Wind Stress with Ocean General Circulation Model. (Oceanographical Research Division, 1989)

第25号　太平洋における海洋諸要素の季節平均分布（海洋研究部，1989)

Seasonal Mean Distribution of Sea Properties in the Pacific. (Oceanographical Research Division, 1989)

第26号　地震前兆現象のデータベース（地震火山研究部，1990）
Database of Earthquake Precursors. (Seismology and Volcanology Research Division, 1990)

第27号　沖縄地方における梅雨期の降水システムの特性（台風研究部，1991）
Characteristics of Precipitation Systems During the Baiu Season in the Okinawa Area. (Typhoon Research Division, 1991)

第28号　気象研究所・予報研究部で開発された非静水圧モデル（猪川元興・斉藤和雄，1991）
Description of a Nonhydrostatic Model Developed at the Forecast Research Department of the MRI. (M. Ikawa and K. Saito, 1991)

第29号　雲の放射過程に関する総合的研究（気候研究部・物理気象研究部・応用気象研究部・気象衛星・観測システム研究部・台風研究部，1992）
A Synthetic Study on Cloud−Radiation Processes. (Climate Research Department, Physical Meteorology Research Department, Applied Meteorology Research Department, Meteorological Satellite and Observation System Research Department, and Typhoon Research Department, 1992)

第30号　大気と海洋・地表とのエネルギー交換過程に関する研究（三上正男・遠藤昌宏・新野　宏・山崎孝治，1992）
Studies of Energy Exchange Processes between the Ocean−Ground Surface and Atmosphere. (M. Mikami, M. Endoh, H. Niino, and K. Yamazaki, 1992)

第31号　降水日の出現頻度からみた日本の季節推移−30年間の日降水量資料に基づく統計−（秋山孝子，1993）
Seasonal Transition in Japan, as Revealed by Appearance Frequency of Precipitating-Days. −Statistics of Daily Precipitation Data During 30 Years−(T. Akiyama, 1993)

第32号　直下型地震予知に関する観測的研究（地震火山研究部，1994）
Observational Study on the Prediction of Disastrous Intraplate Earthquakes. (Seismology and Volcanology Research Department, 1994)

第33号　各種気象観測機器による比較観測（気象衛星・観測システム研究部，1994）
Intercomparisons of Meteorological Observation Instruments. (Meteorological Satellite and Observation System Research Department, 1994)

第34号　硫黄酸化物の長距離輸送モデルと東アジア地域への適用（応用気象研究部，1995）
The Long−Range Transport Model of Sulfur Oxides and Its Application to the East Asian Region. (Applied Meteorology Research Department, 1995)

第35号　ウインドプロファイラーによる気象の観測法の研究（気象衛星・観測システム研究部，1995）
Studies on Wind Profiler Techniques for the Measurements of Winds. (Meteorological Satellite and Observation System Research Department, 1995)

第36号　降水・落下塵中の人工放射性核種の分析法及びその地球化学的研究（地球化学研究部，1996）
Geochemical Studies and Analytical Methods of Anthropogenic Radionuclides in Fallout Samples. (Geochemical Research Department, 1996)

第37号　大気と海洋の地球化学的研究（1995年及び1996年）（地球化学研究部，1998）
Geochemical Study of the Atmosphere and Ocean in 1995 and 1996. (Geochemical Research Department, 1998)

第38号　鉛直２次元非線形問題（金久博忠，1999）
Vertically 2-dmensional Nonlinear Problem, (H. Kanehisa, 1999)

気象研究所技術報告　ISSN 0386-4049

第 39 号

平成12年 2 月29日　発 行

編集兼
発行者　気　象　研　究　所

〒305-0052　茨城県つくば市長峰１－１

TEL. (0298)53-8535

印刷所　株式会社エムディー

〒300-1544 茨城県北相馬郡藤代町大字山王345-1